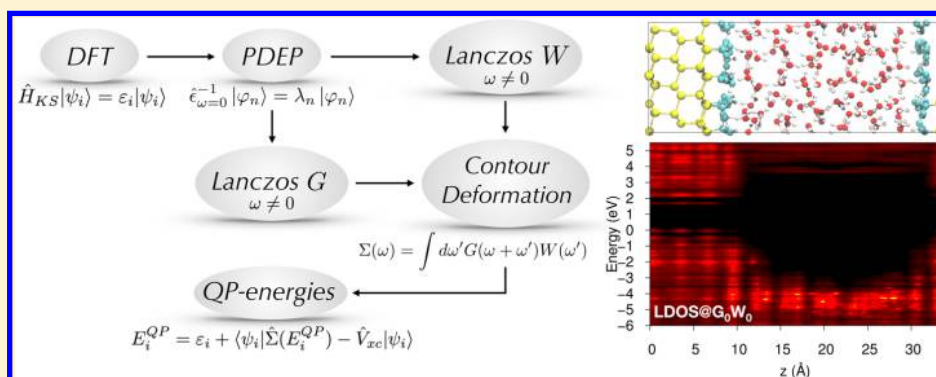


Large Scale GW Calculations

Marco Govoni^{*,†,‡} and Giulia Galli^{*,†,‡}

[†]Institute for Molecular Engineering, The University of Chicago, Chicago, Illinois 60637, United States

[‡]Materials Science Division, Argonne National Laboratory, Argonne, Illinois 60439, United States



ABSTRACT: We present GW calculations of molecules, ordered and disordered solids and interfaces, which employ an efficient contour deformation technique for frequency integration and do not require the explicit evaluation of virtual electronic states nor the inversion of dielectric matrices. We also present a parallel implementation of the algorithm, which takes advantage of separable expressions of both the single particle Green's function and the screened Coulomb interaction. The method can be used starting from density functional theory calculations performed with semilocal or hybrid functionals. We applied the newly developed technique to GW calculations of systems of unprecedented size, including water/semiconductor interfaces with thousands of electrons.

1. INTRODUCTION

The accurate description of the excited state properties of electrons plays an important role in many fields of chemistry, physics, and materials science.¹ For example, the interpretation and prediction of photoemission and optoelectronic spectra of molecules and solids rely on the ability to compute transitions between occupied and virtual electronic states from first-principles, as well as their lifetimes.²

In particular, in the growing field of materials for energy conversion processes—including solar energy conversion by the photovoltaic effect and solar to fuel generation by water photocatalysis—it has become key to develop predictive tools to investigate the excited state properties of nanostructures and nanocomposites and of complex interfaces.^{3–5} The latter include solid/solid and solid/liquid interfaces, for example, between a semiconductor or insulator and water or an electrolyte.^{6–10}

In the last three decades, Density Functional Theory (DFT) has been widely used to compute structural and electronic properties of solids and molecules.^{11–15} Although successful in describing ground state and thermodynamic properties, and in many *ab initio* molecular dynamics studies,^{16,17} DFT with both semilocal and hybrid functionals has failed to accurately describe excited state properties of several materials.¹⁸ However, hybrid functionals have brought great improvement for properties computed with semilocal ones, for example, for defects in semiconductor and oxides.^{19–22} In particular,

hybrid functionals with admixing parameters computed self-consistently have shown good performance in reproducing experimental band gaps and dielectric constants of broad classes of systems.²³ In the case of the electronic properties of surfaces and interfaces (and hence nanostructures), the use of hybrid functionals has in many instances not been satisfactory. Indeed calculations with hybrid functionals yield results for electronic levels that often depend on the mixing parameter chosen for the Hartree–Fock exchange; such parameter is system dependent, and there is no known functional yielding satisfactory results for the electronic properties of interfaces composed of materials with substantially different dielectric properties, as different as those of, for example, water ($\epsilon_\infty = 1.78$)²⁴ and Si ($\epsilon_\infty = 11.9$)²⁵ or water and transition metal oxides of interest for photoelectrodes ($\epsilon_\infty = 5–7$).²⁶

The use of many body perturbation (MBPT) starting from DFT single particle states has proven accurate for several classes of systems,^{27–36} and it appears to be a promising framework to describe complex nanocomposites and heterogeneous interfaces. MBPT for the calculations of photoemission spectra in the GW approximation,³⁷ and of optical spectra by solving approximate forms of the Bethe–Salpeter Equation (BSE),³⁸ is in principle of general applicability; however, its use has been

Received: October 27, 2014

Published: January 12, 2015

greatly limited by computational difficulties in solving the Dyson's equation and the BSE for realistic systems.

Recently, we proposed a method to compute quasi particle energies within the G_0W_0 approximation (i.e., the non-selfconsistent GW approximation) that requires neither the explicit calculation of virtual electronic states nor the inversion of large dielectric matrices.^{39,40} In addition, the method does not use plasmon pole models, but instead, frequency integrations are explicitly performed, and there is one single parameter that controls the accuracy of the computed energies, that is, the number of eigenvectors and eigenvalues used in the spectral decomposition of the dielectric matrix at zero frequency. The method was successfully used to compute the electronic properties of water⁴¹ and aqueous solutions⁴² and of heterogeneous solids,⁵ including crystalline and amorphous samples.⁴⁰

However, the original method contained some numerical approximations in the calculations of the head and wings of the polarizability matrix; most importantly, the correlation self-energy was computed on the imaginary axis and obtained in real space by analytic continuation. Finally, although exhibiting excellent scalability, the method was not yet applied to systems with thousands of electrons, for example, to realistic interfaces, due to the lack of parallelization in its original implementation.

In this paper, we solved all of the problems listed above by (i) eliminating numerical approximations in the calculation of the polarizability, (ii) avoiding the use of an analytic continuation and using efficient contour deformation techniques, (iii) providing a parallel implementation of the algorithm based on separable forms of both the single particle Green function and the screened Coulomb interaction. The method presented here can be used starting from DFT orbitals and energies obtained both with semilocal and hybrid functionals. We applied our technique to the calculation of the electronic properties of systems of unprecedented size, including water/semiconductor interfaces with more than 1000 electrons. These calculations allow one to accurately study states at heterogeneous interfaces and to define an electronic thickness of solid/liquid interfaces using MBPT.

The rest of the paper is organized as follows. Section 2 describes the G_0W_0 methodology that we implemented in a computational package called West. Section 3 presents results for the ionization potentials of closed and open shell molecules and for the electronic structure of crystalline, amorphous, and liquid systems aimed at verifying and validating the algorithm and code West against previous calculations and measurements. Section 4 presents the study of the electronic properties of finite and extended large systems, that is, nanocrystals and solid/liquid interfaces, of interest to photovoltaic and photocatalysis applications, respectively. Our conclusions are reported in Section 5.

2. METHOD

Within DFT, the n -th single particle state $\psi_{n\mathbf{k}\sigma}$ and energy $\epsilon_{n\mathbf{k}\sigma}$ of a system of interacting electrons is obtained by solving the Kohn–Sham (KS) equation:^{11–15}

$$\hat{H}_{\text{KS}}^\sigma \psi_{n\mathbf{k}\sigma} = \epsilon_{n\mathbf{k}\sigma} \psi_{n\mathbf{k}\sigma} \quad (1)$$

where $\hat{H}_{\text{KS}}^\sigma = \hat{T} + \hat{V}_{\text{ion}} + \hat{V}_{\text{H}} + \hat{V}_{\text{xc}}^\sigma$ is the KS Hamiltonian, \hat{T} is the kinetic energy operator, and \hat{V}_{ion} , \hat{V}_{H} , and $\hat{V}_{\text{xc}}^\sigma$ are the ionic, Hartree, and exchange–correlation potential operators, respectively. The indexes \mathbf{k} and σ label a wavevector within the first

Brillouin zone (BZ) and spin polarization, respectively. Here, we consider collinear spin, that is, decoupled up and down spins.

In a fashion similar to eq 1 one may obtain quasiparticle (QP) states $\psi_{n\mathbf{k}\sigma}^{\text{QP}}$ and QP energies $E_{n\mathbf{k}\sigma}^{\text{QP}}$ by solving the equation:

$$\hat{H}_{\text{QP}}^\sigma \psi_{n\mathbf{k}\sigma}^{\text{QP}} = E_{n\mathbf{k}\sigma}^{\text{QP}} \psi_{n\mathbf{k}\sigma}^{\text{QP}} \quad (2)$$

where the QP Hamiltonian $\hat{H}_{\text{QP}}^\sigma$ is formally obtained by replacing, in eq 1, the exchange–correlation potential operator with the electron self-energy operator $\Sigma^\sigma = iG^\sigma W\Gamma$; G^σ is the interacting one-particle Green's function, W is the screened Coulomb interaction, and Γ is the vertex operator.^{28,43} All quantities entering the definition of the self-energy are interdependent and can be obtained self-consistently adopting the scheme suggested by L. Hedin.^{44–46} In the GW approximation, Γ is set equal to the identity, which yields the following expression for the electron self-energy:⁴⁷

$$\Sigma^\sigma(\mathbf{r}, \mathbf{r}'; \omega) = i \int_{-\infty}^{+\infty} \frac{d\omega'}{2\pi} G^\sigma(\mathbf{r}, \mathbf{r}'; \omega + \omega') W_{\text{RPA}}(\mathbf{r}, \mathbf{r}'; \omega') \quad (3)$$

where W_{RPA} is the screened Coulomb interaction obtained in the random phase approximation (RPA). Due to the non-locality and the frequency dependence of the electron self-energy, a self-consistent solution of eq 2 is computationally very demanding also for relatively small systems, containing tens of electrons, and usually one evaluates QP energies $E_{n\mathbf{k}\sigma}^{\text{QP}}$ perturbatively:

$$E_{n\mathbf{k}\sigma}^{\text{QP}} = \epsilon_{n\mathbf{k}\sigma} + \langle \psi_{n\mathbf{k}\sigma} | (\hat{H}_{\text{QP}}^\sigma - \hat{H}_{\text{KS}}^\sigma) | \psi_{n\mathbf{k}\sigma} \rangle \quad (4)$$

$$= \epsilon_{n\mathbf{k}\sigma} + \langle \psi_{n\mathbf{k}\sigma} | \hat{\Sigma}^\sigma(E_{n\mathbf{k}\sigma}^{\text{QP}}) | \psi_{n\mathbf{k}\sigma} \rangle - \langle \psi_{n\mathbf{k}\sigma} | \hat{V}_{\text{xc}}^\sigma | \psi_{n\mathbf{k}\sigma} \rangle \quad (5)$$

We note that $E_{n\mathbf{k}\sigma}^{\text{QP}}$ enters both the left and right-hand side of eq 5, whose solution is usually obtained recursively, e.g. with root-finding algorithms such as the secant method. The use of eq 5 to evaluate QP energies from KS states and of the corresponding KS wave functions is known as the G_0W_0 approximation.

Within G_0W_0 , using the Lehmann's representation, the Green's function is

$$G_{\text{KS}}^\sigma(\mathbf{r}, \mathbf{r}'; \omega) = - \sum_n \int_{\text{BZ}} \frac{d\mathbf{k}}{(2\pi)^3} \frac{\psi_{n\mathbf{k}\sigma}(\mathbf{r}) \psi_{n\mathbf{k}\sigma}^*(\mathbf{r}')}{\epsilon_{n\mathbf{k}\sigma} - \omega - i\eta \text{sign}(\epsilon_{n\mathbf{k}\sigma} - \epsilon_{\text{F}})} \quad (6)$$

where η is a small positive quantity and ϵ_{F} is the Fermi energy. In eq 6, we used the subscript KS to indicate that the Green's function is evaluated using the KS orbitals obtained by solving eq 1.

In refs 39 and 40, an algorithm was introduced to compute the self-energy matrix elements of eq 5 without the need to evaluate explicitly empty (virtual) electronic states, by using a technique called projective eigendecomposition of the dielectric screening (PDEP). A diagram of the method is reported in Figure 1. After KS single particle orbitals and energies are obtained using semilocal or hybrid functionals, the screened Coulomb interaction is computed using a basis set built from the eigenpotentials of the static dielectric matrix at zero frequency. In this way, W_{RPA} entering eq 3 is expressed in a separable form, similar to that of G_{KS}^σ in eq 6. In the following sections, we describe in detail all the steps outlined in Figure 1. The separable form of W_{RPA} is given in Section 2.1. Calculation of the polarizability and the spectral decomposition of the dielectric matrix are described in Sections 2.2 and 2.3, respectively. Matrix elements of G_{KS}^σ and W_{RPA} are then

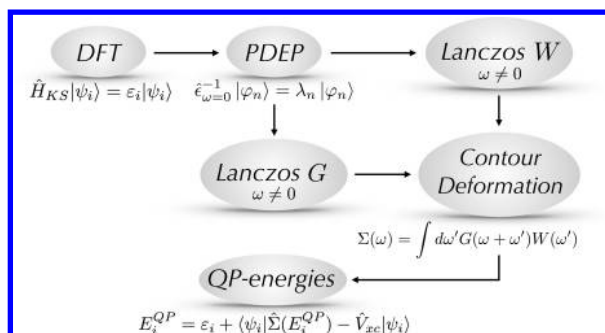


Figure 1. (Color online) Schematic representation of the steps involved in the calculations of quasiparticle (QP) energies, within the G_0W_0 approximation, using the method proposed in this work. The KS energies (ϵ_i) and occupied orbitals (ψ_i) computed at the DFT level are input to the PDEP algorithm, which is used to iteratively diagonalize the static dielectric matrix (ϵ^{-1}) at zero frequency. The set of eigenvectors $\{\varphi_n\}$ constitutes the basis set used to compute both G and W at finite frequencies with the Lanczos algorithm. The frequency integration of eq 3 is carried out using the contour deformation technique. The frequency dependent matrix elements of the electron self-energy are thus obtained and introduced in eq 5 to compute the QP energies E_i^{QP} .

obtained without the explicit use of empty electronic states and simultaneously at several frequencies by using a deflated Lanczos technique, described in Section 2.4. Finally, the frequency integration is carried out by introducing a contour deformation method, as described in Section 2.5. The use of the analytic continuation used in the original method of refs 39 and 40 is thus avoided.

2.1. Separable Form of the Screened Coulomb Interaction. In order to solve eq 5 and obtain QP energies, one needs to compute the matrix elements of the electron self-energy between KS states, which in the G_0W_0 approximation is given by eq 3. The Green's function may be expressed in a fully separable form using its Lehmann's representation, eq 6. However, W_{RPA} is not trivially separable; it is given as the sum of two terms:

$$W_{\text{RPA}}(\mathbf{r}, \mathbf{r}'; \omega) = v(\mathbf{r}, \mathbf{r}') + W_p(\mathbf{r}, \mathbf{r}'; \omega) \quad (7)$$

where $v(\mathbf{r}, \mathbf{r}') = e^2/|\mathbf{r} - \mathbf{r}'|$ is the bare Coulomb interaction⁴⁸ and W_p is a nonlocal and frequency dependent function. Using eq 7, we write the self-energy as the sum of two contributions $\Sigma^\sigma = \Sigma_X^\sigma + \Sigma_C^\sigma$ where only the latter depends on the frequency:

$$\Sigma_X^\sigma(\mathbf{r}, \mathbf{r}') = i \int_{-\infty}^{+\infty} \frac{d\omega'}{2\pi} G_{\text{KS}}^\sigma(\mathbf{r}, \mathbf{r}'; \omega + \omega') v(\mathbf{r}, \mathbf{r}') \quad (8)$$

$$= - \sum_{n=1}^{N_{\text{occ}}^\sigma} \int_{\text{BZ}} \frac{d\mathbf{k}}{(2\pi)^3} \psi_{n\mathbf{k}\sigma}(\mathbf{r}) v(\mathbf{r}, \mathbf{r}') \psi_{n\mathbf{k}\sigma}^*(\mathbf{r}') \quad (9)$$

N_{occ}^σ is the number of occupied states with spin σ ; Σ_X^σ is usually called exchange self-energy because it is formally equivalent to the Fock exact exchange operator;⁴⁹

$$\Sigma_C^\sigma(\mathbf{r}, \mathbf{r}'; \omega) = i \int_{-\infty}^{+\infty} \frac{d\omega'}{2\pi} G_{\text{KS}}^\sigma(\mathbf{r}, \mathbf{r}'; \omega + \omega') W_p(\mathbf{r}, \mathbf{r}'; \omega') \quad (10)$$

Σ_C^σ is referred to as correlation self-energy. Using eqs 8–10, the QP Hamiltonian of eq 2 may be expressed as

$$\hat{H}_{\text{QP}}^\sigma(\omega) = \hat{T} + \hat{V}_{\text{ion}} + \hat{V}_{\text{HF}}^\sigma + \hat{\Sigma}_C^\sigma(\omega) \quad (11)$$

where $\hat{V}_{\text{HF}}^\sigma$ is the Hartree–Fock potential operator. The ionic potential \hat{V}_{ion} is treated within the pseudopotential approach.⁵⁰

In this work, we express W_p in a separable form by adopting the projective dielectric eigendecomposition (PDEP) technique, proposed in refs 51 and 52, and we use a plane wave basis set to express the single particle wave functions and charge density, within periodic boundary conditions:

$$\psi_{n\mathbf{k}\sigma}(\mathbf{r}) = e^{i\mathbf{k}\mathbf{r}} u_{n\mathbf{k}\sigma}(\mathbf{r}) = \sum_{\mathbf{G}} c_{n\mathbf{k}\sigma}(\mathbf{G}) e^{i(\mathbf{k}+\mathbf{G})\cdot\mathbf{r}} \quad (12)$$

where $c_{n\mathbf{k}\sigma}(\mathbf{G}) = 1/\Omega \int_{\Omega} d\mathbf{r} u_{n\mathbf{k}\sigma}(\mathbf{r}) e^{-i\mathbf{G}\cdot\mathbf{r}}$, \mathbf{G} is a reciprocal lattice vector, and Ω is the unit cell volume. In eq 12 all reciprocal lattice vectors such that $|\mathbf{k} + \mathbf{G}|^2 < E_{\text{cutwfc}}$ are included in the summation. Using a plane wave description also for W_p we have

$$W_{\text{RPA}}(\mathbf{r}, \mathbf{r}'; \omega) = \int_{\text{BZ}} \frac{d\mathbf{q}}{(2\pi)^3} \sum_{\mathbf{G}\mathbf{G}'} e^{i(\mathbf{q}+\mathbf{G})\cdot\mathbf{r}} [v_{\mathbf{G}\mathbf{G}'} + W_{\mathbf{G}\mathbf{G}'}^p(\mathbf{q}; \omega)] \times e^{-i(\mathbf{q}+\mathbf{G}')\cdot\mathbf{r}'} \quad (13)$$

where $v_{\mathbf{G}\mathbf{G}'} = (4\pi e^2/|\mathbf{q}+\mathbf{G}|^2) \delta_{\mathbf{G}\mathbf{G}'}$ (δ is the Kronecker delta) and

$$W_{\mathbf{G}\mathbf{G}'}^p(\mathbf{q}; \omega) = \frac{\sqrt{4\pi e^2}}{|\mathbf{q} + \mathbf{G}|} \bar{\chi}_{\mathbf{G}\mathbf{G}'}(\mathbf{q}; \omega) \frac{\sqrt{4\pi e^2}}{|\mathbf{q} + \mathbf{G}'|} \quad (14)$$

In eq 14, we have introduced the symmetrized reducible polarizability $\bar{\chi}$, related to the symmetrized inverse dielectric matrix $\bar{\epsilon}^{-1}$ by the relation:

$$\bar{\epsilon}_{\mathbf{G}\mathbf{G}'}^{-1}(\mathbf{q}; \omega) = \delta_{\mathbf{G}\mathbf{G}'} + \bar{\chi}_{\mathbf{G}\mathbf{G}'}(\mathbf{q}; \omega) \quad (15)$$

The symmetrized form $\bar{\chi}$ of the polarizability χ is

$$\bar{\chi}_{\mathbf{G}\mathbf{G}'} = \frac{\sqrt{4\pi e^2}}{|\mathbf{q} + \mathbf{G}|} \chi_{\mathbf{G}\mathbf{G}'} \frac{\sqrt{4\pi e^2}}{|\mathbf{q} + \mathbf{G}'|} \quad (16)$$

The reducible polarizability χ is related to the irreducible polarizability χ_0 by the Dyson's equation, which within the RPA reads:

$$\chi_{\mathbf{G}\mathbf{G}'} = \chi_{\mathbf{G}\mathbf{G}'}^0 + \sum_{\mathbf{G}_1, \mathbf{G}_2} \chi_{\mathbf{G}\mathbf{G}_1}^0 v_{\mathbf{G}_1 \mathbf{G}_2} \chi_{\mathbf{G}_2 \mathbf{G}'} \quad (17)$$

or in terms of symmetrized polarizabilities:

$$\bar{\chi} = (1 - \bar{\chi}^0)^{-1} \bar{\chi}^0 \quad (18)$$

Within a plane wave representation, each quantity in eq 18 is a matrix of dimension N_{pw}^2 , and in principle, $\bar{\chi}$ can be obtained from $\bar{\chi}^0$ via simple linear algebra operations. In practice, the matrices of eq 18 may contain millions of rows and columns for realistic systems; for example, for a silicon nanocrystal with 465 atoms, placed in a cubic box of edge 90 bohr, 1.5 million plane waves are needed in the expansion of eq 12 with $E_{\text{cutwfc}} = 25$ Ry. It is thus important to find alternative representations of $\bar{\chi}$ and reduce the number of elements to compute. One could think of a straightforward spectral decomposition:

$$\bar{\chi}_{\mathbf{G}\mathbf{G}'}(\mathbf{q}; \omega) = \sum_{i=1}^{N_{\text{pdep}}} \varphi_i(\mathbf{q} + \mathbf{G}; \omega) \lambda_i(\mathbf{q}; \omega) \varphi_i^*(\mathbf{q} + \mathbf{G}'; \omega) \quad (19)$$

where φ_i and λ_i are the eigenvectors and eigenvalues of $\bar{\chi}$, respectively. Unfortunately this strategy is still too demanding from a computational standpoint, as it implies finding eigenvectors and eigenvalues at multiple frequencies.

A computationally more tractable representation may be obtained using the spectral decomposition of $\bar{\chi}_0$ at $\omega = 0$. As apparent from eq 18, eigenvectors of $\bar{\chi}$ are also eigenvectors of $\bar{\chi}^0$; the latter is easier to iteratively diagonalize than $\bar{\chi}$, and the frequency dependency may be dealt with iterative techniques, starting from the solution at $\omega = 0$, as discussed in Section 2.4. Therefore, we proceed by solving the secular equation for $\bar{\chi}^0$ only at $\omega = 0$, generating what we call the PDEP basis set $\{|\varphi_i\rangle: i = 1, N_{\text{pdep}}\}$, which is used throughout this work to represent the polarizability $\bar{\chi}$:

$$\bar{\chi}_{\mathbf{GG}'}(\mathbf{q}; \omega) = \sum_{i,j=1}^{N_{\text{pdep}}} \varphi_i(\mathbf{q} + \mathbf{G}) \Lambda_{ij}(\mathbf{q}; \omega) \varphi_j^*(\mathbf{q} + \mathbf{G}') \quad (20)$$

Here, $\Lambda_{ij}(\mathbf{q}; \omega)$ is a matrix of dimension N_{pdep}^2 . In general $N_{\text{pdep}} \ll N_{\text{pw}}$,^{51,52} leading to substantial computational savings.⁵³ The N_{pdep} functions φ_i may be computed by solving the Sternheimer equation,⁵⁴ without explicitly evaluating empty (virtual) electronic states. In addition, N_{pdep} turns out to be the only parameter that controls the accuracy of the expansion in eq 20. The details of the derivation of the PDEP basis set are given in Section 2.3. We note that alternative basis sets, based on the concepts related to maximally localized Wannier functions, have been proposed in the literature to reduce the dimensionality of the polarizability matrices.⁵⁵

By defining $\tilde{\varphi}_i(\mathbf{q} + \mathbf{G}) = \sqrt{4\pi e^2} \varphi_i(\mathbf{q} + \mathbf{G}) / |\mathbf{q} + \mathbf{G}|$, we formally obtain the desired separable form for W_p :

$$W_p(\mathbf{r}, \mathbf{r}'; \omega) = \int_{\text{BZ}} \frac{d\mathbf{q}}{(2\pi)^3} \sum_{i,j=1}^{N_{\text{pdep}}} \tilde{\varphi}_i(\mathbf{q}; \mathbf{r}) \Lambda_{ij}(\mathbf{q}; \omega) \tilde{\varphi}_j^*(\mathbf{q}; \mathbf{r}') \quad (21)$$

We now focus the derivation on large systems where the BZ can be sampled only at the Γ point. The scaling operation used to define $\tilde{\varphi}_i$ is divergent in the long wavelength limit ($\mathbf{q} \rightarrow \mathbf{0}$) and for $\mathbf{G} = \mathbf{0}$. However, such divergence can be integrated yielding:

$$W_p(\mathbf{r}, \mathbf{r}'; \omega) = \Xi(\omega) + \frac{1}{\Omega} \sum_{i,j=1}^{N_{\text{pdep}}} \tilde{\varphi}_i(\mathbf{r}) \Lambda_{ij}(\omega) \tilde{\varphi}_j^*(\mathbf{r}') \quad (22)$$

where

$$\Xi(\omega) = 4\pi e^2 \int_{R_{\mathbf{q}=\mathbf{0}}} \frac{d\mathbf{q}}{(2\pi)^3} \frac{\bar{\chi}_{\mathbf{00}}(\mathbf{q}; \omega)}{q^2} \quad (23)$$

In eq 23, the integration is evaluated on the region $R_{\mathbf{q}=\mathbf{0}}$ of the BZ enclosing the Γ -point (i.e., $\mathbf{q} = \mathbf{0}$).⁵⁶

In the $\mathbf{q} \rightarrow \mathbf{0}$ limit, we can now write the matrix elements of Σ_C^σ using (i) the separable form of W_p of eq 22 and (ii) the expression of $G_{\mathbf{KS}}$, given in eq 6, in terms of projector operators:

$$\hat{G}_{\mathbf{KS}}^\sigma(\omega) = \int_{\text{BZ}} \frac{d\mathbf{k}}{(2\pi)^3} \hat{P}_v^{\mathbf{k}\sigma} \hat{O}_{\mathbf{KS}}^\sigma(\omega - i\eta) \hat{P}_v^{\mathbf{k}\sigma} + \int_{\text{BZ}} \frac{d\mathbf{k}}{(2\pi)^3} \hat{P}_c^{\mathbf{k}\sigma} \hat{O}_{\mathbf{KS}}^\sigma(\omega + i\eta) \hat{P}_c^{\mathbf{k}\sigma} \quad (24)$$

where

$$\hat{O}_{\mathbf{KS}}^\sigma(\omega) = -(\hat{H}_{\mathbf{KS}}^\sigma - \omega)^{-1} \quad (25)$$

$\hat{P}_v^{\mathbf{k}\sigma} = \sum_{n=1}^{N_{\text{occ}}} |\psi_{n\mathbf{k}\sigma}\rangle \langle \psi_{n\mathbf{k}\sigma}|$ and $\hat{P}_c^{\mathbf{k}\sigma} = \sum_{n=N_{\text{occ}}+1}^{+\infty} |\psi_{n\mathbf{k}\sigma}\rangle \langle \psi_{n\mathbf{k}\sigma}|$ are the projector operator over the occupied and unoccupied manifold of states belonging to \mathbf{k} -point \mathbf{k} and spin σ , respectively. In the present formulation, we considered integer

occupation numbers and only the dielectric response given by interband transitions.⁵⁷ Hence, we have

$$\langle \psi_{n\mathbf{k}\sigma} | \Sigma_C^\sigma(\omega) | \psi_{n\mathbf{k}\sigma} \rangle = A_{n\mathbf{k}\sigma}(\omega) + B_{n\mathbf{k}\sigma}(\omega) + C_{n\mathbf{k}\sigma}(\omega) + D_{n\mathbf{k}\sigma}(\omega) \quad (26)$$

where $A_{n\mathbf{k}\sigma}$ and $C_{n\mathbf{k}\sigma}$ ($B_{n\mathbf{k}\sigma}$ and $D_{n\mathbf{k}\sigma}$) are contributions to the correlation self-energy originating from occupied (empty) states:

$$A_{n\mathbf{k}\sigma}(\omega) = i \int_{-\infty}^{+\infty} \frac{d\omega'}{2\pi} \Xi(\omega') \times \langle \psi_{n\mathbf{k}\sigma} | \hat{P}_v^{\mathbf{k}\sigma} \hat{O}_{\mathbf{KS}}^\sigma(\omega + \omega' - i\eta) \hat{P}_v^{\mathbf{k}\sigma} | \psi_{n\mathbf{k}\sigma} \rangle \quad (27)$$

$$B_{n\mathbf{k}\sigma}(\omega) = i \int_{-\infty}^{+\infty} \frac{d\omega'}{2\pi} \Xi(\omega') \times \langle \psi_{n\mathbf{k}\sigma} | \hat{P}_c^{\mathbf{k}\sigma} \hat{O}_{\mathbf{KS}}^\sigma(\omega + \omega' + i\eta) \hat{P}_c^{\mathbf{k}\sigma} | \psi_{n\mathbf{k}\sigma} \rangle \quad (28)$$

$$C_{n\mathbf{k}\sigma}(\omega) = \frac{i}{\Omega} \int_{-\infty}^{+\infty} \frac{d\omega'}{2\pi} \sum_{i,j=1}^{N_{\text{pdep}}} \Lambda_{ij}(\omega') \times \langle \varphi_{n\mathbf{k}\sigma}^i | \hat{P}_v^{\mathbf{k}\sigma} \hat{O}_{\mathbf{KS}}^\sigma(\omega + \omega' - i\eta) \hat{P}_v^{\mathbf{k}\sigma} | \varphi_{n\mathbf{k}\sigma}^j \rangle \quad (29)$$

$$D_{n\mathbf{k}\sigma}(\omega) = \frac{i}{\Omega} \int_{-\infty}^{+\infty} \frac{d\omega'}{2\pi} \sum_{i,j=1}^{N_{\text{pdep}}} \Lambda_{ij}(\omega') \times \langle \varphi_{n\mathbf{k}\sigma}^i | \hat{P}_c^{\mathbf{k}\sigma} \hat{O}_{\mathbf{KS}}^\sigma(\omega + \omega' + i\eta) \hat{P}_c^{\mathbf{k}\sigma} | \varphi_{n\mathbf{k}\sigma}^j \rangle \quad (30)$$

We have defined $\varphi_{n\mathbf{k}\sigma}^i(\mathbf{r}) = \psi_{n\mathbf{k}\sigma}(\mathbf{r}) \tilde{\varphi}_i^*(\mathbf{r})$. The quantities $A_{n\mathbf{k}\sigma}$, $B_{n\mathbf{k}\sigma}$, $C_{n\mathbf{k}\sigma}$ and $D_{n\mathbf{k}\sigma}$ entering eq 26 are now in a form where iterative techniques (see Section 2.4) can be applied to obtain the matrix elements of the correlation self-energy. Moreover, because of the completeness of energy eigenstates ($\hat{P}_c^{\mathbf{k}\sigma} = 1 - \hat{P}_v^{\mathbf{k}\sigma}$), we may compute all quantities in eqs 27–30 considering only occupied states. The integration over the frequency domain will be discussed in Section (2.5).

2.2. Polarizability within the Random Phase Approximation. Here, we discuss how to compute the polarizability $\bar{\chi}$ from $\bar{\chi}^0$ within the RPA, in the long wavelength limit ($\mathbf{q} \rightarrow \mathbf{0}$), without explicitly evaluating electronic empty states. The Fourier components of the symmetrized irreducible polarizability $\bar{\chi}^0$ are given by the Adler–Wiser expression,^{58,59} which contains an explicit summation over unoccupied states:

$$\bar{\chi}_{\mathbf{GG}'}^0(\mathbf{q}; \omega) = -4\pi e^2 \sum_{\sigma} \sum_{n=1}^{N_{\text{occ}}} \sum_{m=N_{\text{occ}}+1}^{+\infty} \int_{\text{BZ}} \frac{d\mathbf{k}}{(2\pi)^3} \times \frac{\rho_{mn\mathbf{k}\sigma}^*(\mathbf{q}, \mathbf{G}) \rho_{mn\mathbf{k}\sigma}(\mathbf{q}, \mathbf{G}')}{|\mathbf{q} + \mathbf{G}| |\mathbf{q} + \mathbf{G}'|} \left[\frac{1}{\epsilon_{m\mathbf{k}\sigma} - \epsilon_{n\mathbf{k}-\mathbf{q}\sigma} + \omega - i\eta} + \frac{1}{\epsilon_{m\mathbf{k}\sigma} - \epsilon_{n\mathbf{k}-\mathbf{q}\sigma} - \omega - i\eta} \right] \quad (31)$$

where the matrix element

$$\rho_{mn\mathbf{k}\sigma}(\mathbf{q}, \mathbf{G}) = \langle \psi_{m\mathbf{k}\sigma} | e^{i(\mathbf{q}+\mathbf{G})\cdot\mathbf{r}} | \psi_{n\mathbf{k}-\mathbf{q}\sigma} \rangle \quad (32)$$

is often referred to as oscillator strength; it has the following properties:

$$\rho_{mn\mathbf{k}\sigma}(\mathbf{q}, \mathbf{G} = \mathbf{0})|_{\mathbf{q} \rightarrow \mathbf{0}} = \delta_{nm} \quad (33)$$

$$\nabla_{\mathbf{q}} \rho_{mn\mathbf{k}\sigma}(\mathbf{q}, \mathbf{G} = \mathbf{0})|_{\mathbf{q} \rightarrow \mathbf{0}} = i \langle \psi_{m\mathbf{k}\sigma} | \mathbf{r} | \psi_{n\mathbf{k}\sigma} \rangle \quad (34)$$

Following refs 60 and 61, we partition the polarizability of eq 31 into head ($\mathbf{G} = \mathbf{G}' = \mathbf{0}$), wings ($\mathbf{G} = \mathbf{0}, \mathbf{G}' \neq \mathbf{0}$, or $\mathbf{G} \neq \mathbf{0}, \mathbf{G}' = \mathbf{0}$) and body ($\mathbf{G} \neq \mathbf{0}$ and $\mathbf{G}' \neq \mathbf{0}$) elements. The $\mathbf{q} \rightarrow \mathbf{0}$ limit of the body, which we call $B_{GG'}$, is analytic, while the limits of the head and wings are nonanalytic; that is, they depend on the Cartesian direction along which the limit is performed. The long wavelength limits of the head, body, and wings of the polarizability matrix are summarized in Table 1. Using the PDEP basis set, we obtain

$$U_{\alpha j}(\omega) = \sum_{\mathbf{G}'} U_{\alpha \mathbf{G}'}(\omega) \varphi_j(\mathbf{G}') \quad (35)$$

$$B_{ij}(\omega) = \sum_{\mathbf{G}\mathbf{G}'} \varphi_i^*(\mathbf{G}) B_{\mathbf{G}\mathbf{G}'}(\omega) \varphi_j(\mathbf{G}') \quad (36)$$

Table 1. Polarizability in the Long Wavelength Limit

$\bar{\chi}_{\mathbf{G}\mathbf{G}'}^0(\mathbf{q} \rightarrow \mathbf{0}; \omega)$	$\mathbf{G}' = \mathbf{0}$	$\mathbf{G}' \neq \mathbf{0}$
$\mathbf{G} = \mathbf{0}$	$\sum_{\alpha\beta} q_{\alpha} F_{\alpha\beta}(\omega) q_{\beta} / q^2$	$-i \sum_{\alpha} q_{\alpha} U_{\alpha \mathbf{G}'}(\omega) / q$
$\mathbf{G} \neq \mathbf{0}$	$i \sum_{\beta} U_{\mathbf{G}\beta}(\omega) q_{\beta} / q$	$B_{\mathbf{G}\mathbf{G}'}(\omega)$

We can now express all the quantities in Table 1 without any explicit summation over empty (virtual) states:

$$F_{\alpha\beta}(\omega) = \sum_{\sigma} \sum_{n=1}^{N_{\text{occ}}^{\sigma}} \int_{\text{BZ}} \frac{d\mathbf{k}}{(2\pi)^3} \langle \xi_{n\mathbf{k}\sigma}^{\alpha} | \hat{P}_c^{\mathbf{k}\sigma} \times [\hat{O}_{\text{KS}}^{\sigma}(\epsilon_{n\mathbf{k}\sigma} - \omega + i\eta) + \hat{O}_{\text{KS}}^{\sigma}(\epsilon_{n\mathbf{k}\sigma} + \omega + i\eta)] | \xi_{n\mathbf{k}\sigma}^{\beta} \rangle \quad (37)$$

$$U_{\alpha j}(\omega) = \sum_{\sigma} \sum_{n=1}^{N_{\text{occ}}^{\sigma}} \int_{\text{BZ}} \frac{d\mathbf{k}}{(2\pi)^3} \langle \xi_{n\mathbf{k}\sigma}^{\alpha} | \hat{P}_c^{\mathbf{k}\sigma} \times [\hat{O}_{\text{KS}}^{\sigma}(\epsilon_{n\mathbf{k}\sigma} - \omega + i\eta) + \hat{O}_{\text{KS}}^{\sigma}(\epsilon_{n\mathbf{k}\sigma} + \omega + i\eta)] | \xi_{n\mathbf{k}\sigma}^j \rangle \quad (38)$$

$$U_{ij}(\omega) = \sum_{\sigma} \sum_{n=1}^{N_{\text{occ}}^{\sigma}} \int_{\text{BZ}} \frac{d\mathbf{k}}{(2\pi)^3} \langle \xi_{n\mathbf{k}\sigma}^i | \hat{P}_c^{\mathbf{k}\sigma} \times [\hat{O}_{\text{KS}}^{\sigma}(\epsilon_{n\mathbf{k}\sigma} - \omega + i\eta) + \hat{O}_{\text{KS}}^{\sigma}(\epsilon_{n\mathbf{k}\sigma} + \omega + i\eta)] | \xi_{n\mathbf{k}\sigma}^j \rangle \quad (39)$$

$$B_{ij}(\omega) = \sum_{\sigma} \sum_{n=1}^{N_{\text{occ}}^{\sigma}} \int_{\text{BZ}} \frac{d\mathbf{k}}{(2\pi)^3} \langle \xi_{n\mathbf{k}\sigma}^i | \hat{P}_c^{\mathbf{k}\sigma} \times [\hat{O}_{\text{KS}}^{\sigma}(\epsilon_{n\mathbf{k}\sigma} - \omega + i\eta) + \hat{O}_{\text{KS}}^{\sigma}(\epsilon_{n\mathbf{k}\sigma} + \omega + i\eta)] | \xi_{n\mathbf{k}\sigma}^j \rangle \quad (40)$$

Note that the greek letters α and β identify Cartesian directions, while the roman letters i and j label the eigenvectors of $\bar{\chi}^0$ at $\omega = 0$, that is, the elements of the PDEP basis set. We have also defined the auxiliary functions $\xi_{n\mathbf{k}\sigma}^i(\mathbf{r}) = \psi_{n\mathbf{k}\sigma}(\mathbf{r}) \tilde{\varphi}_i(\mathbf{r})$ and $\xi_{n\mathbf{k}\sigma}^{\alpha}(\mathbf{r}) = \sqrt{4\pi e^2} \hat{P}_c^{\mathbf{k}\sigma} r_{\alpha} \psi_{n\mathbf{k}\sigma}$. Within periodic boundary conditions the position operator is ill-defined and $\xi_{n\mathbf{k}\sigma}^{\alpha}(\mathbf{r})$ is obtained by solving the linear system

$$(\hat{H}_{\text{KS}}^{\sigma} - \epsilon_{n\mathbf{k}\sigma}) | \xi_{n\mathbf{k}\sigma}^{\alpha} \rangle = \sqrt{4\pi e^2} \hat{P}_c^{\mathbf{k}\sigma} [\hat{H}_{\text{KS}}^{\sigma}, r_{\alpha}] | \psi_{n\mathbf{k}\sigma} \rangle \quad (41)$$

where the commutator of the KS Hamiltonian with the position operator includes the contribution of the nonlocal

potential.^{60,61} Once $\bar{\chi}^0$ is obtained, $\bar{\chi}$ is computed using eq 18.

The quantities required to evaluate eq 26 are the following:⁶²

$$\Xi(\omega) = \frac{1 - k(\omega)}{k(\omega)} \int_{R_{\mathbf{q}=0}} \frac{d\mathbf{q}}{(2\pi)^3} \frac{4\pi e^2}{|\mathbf{q}|^2} \quad (42)$$

$$\Lambda(\omega) = [\mathbf{1} - \mathbf{B}(\omega)]^{-1} \mathbf{B}(\omega) + \frac{1}{k(\omega)} [\mathbf{1} - \mathbf{B}(\omega)]^{-1} \boldsymbol{\mu}(\omega) [\mathbf{1} - \mathbf{B}(\omega)]^{-1} \quad (43)$$

with $k(\omega) = 1 - f(\omega) - \text{Tr}\{\boldsymbol{\mu}(\omega)[\mathbf{1} - \mathbf{B}(\omega)]^{-1}\}$; $f(\omega) = 1/3(\sum_{\alpha} F_{\alpha\alpha}(\omega))$; and the matrix elements of $\boldsymbol{\mu}_{ij}(\omega) = 1/3(\sum_{\alpha} U_{i\alpha}(\omega) U_{\alpha j}(\omega))$. In eq 43 the bold symbols denote matrices of dimension N_{pdep}^2 . In order to compute the matrix elements of the correlation self-energy, eq 26, we need to evaluate $\Xi(\omega)$ and $\Lambda(\omega)$, namely, the head and body of the $\bar{\chi}$ operator. These are easily obtained via linear algebra operations from $F_{\alpha\beta}(\omega)$, $U_{\alpha j}(\omega)$, $U_{ij}(\omega)$, and $B_{ij}(\omega)$.

By replacing explicit summations over unoccupied states with projection operations, eqs 37–40 may be evaluated using linear equation solvers and (owing to the completeness of the energy eigenstates) the calculation of polarizabilities is carried out without the explicit evaluation of the virtual states. In a similar fashion, one obtains the auxiliary functions $\xi_{n\mathbf{k}\sigma}^{\alpha}(\mathbf{r})$ in eq 41 and the PDEP basis set as described in Section 2.3. We note that other approaches were developed in the literature^{63–66} to improve the efficiency of G_0W_0 calculations by avoiding the calculation of virtual states, or by limiting the number of virtual states to be computed. However, such approaches did not make use of the spectral decomposition of the irreducible polarizability to obtain the reducible polarizability, but instead inverted explicitly large matrices. Specifically, in Reining et al.⁶⁷ the Sternheimer equation was used to obtain the irreducible polarizability without virtual states, and then, a plasmon pole model was adopted to compute the dielectric response as a function of frequency. In Giustino et al.⁶⁸ the Sternheimer equation was used as well to obtain the irreducible polarizability without computing virtual states; the polarizability matrix was then inverted numerically, and either a plasmon pole model or a Padé expansion were used to treat the frequency dependence. In our approach, we avoided large matrix inversion by using the PDEP basis set to express all polarizability matrices. Finally, we note that an additional advantage of our approach is that eqs 37–40 may be computed using a deflated Lanczos algorithm for multiple values of the frequency, as discussed in Section 2.4. A Lanczos algorithm was also used by Soininen et al.⁶⁹ to iteratively include local field effects in RPA Hamiltonians and avoid explicit inversion of large matrices. However, the authors of ref 69 computed explicitly virtual states.

2.3. Projective Dielectric Eigenpotential (PDEP) Basis Set. We now describe in detail how to obtain the PDEP basis set $\{|\varphi_i\rangle; i = 1, N_{\text{pdep}}\}$ introduced in eq 20; each function φ_i is computed by the iterative diagonalization procedure, summarized in Figure 2, the procedure is initiated by building an orthonormal set of N_{pdep} basis vectors, for example, with random components. The N_{pdep} Sternheimer equations are solved in parallel, where the perturbation is given by the i -th basis set vector $\tilde{\varphi}_i(r)$. In particular, given a perturbation \hat{V}_i^{pert} , the linear variation $|\Delta\psi_{n\mathbf{k}\sigma}^i\rangle$ of the occupied eigenstates of the

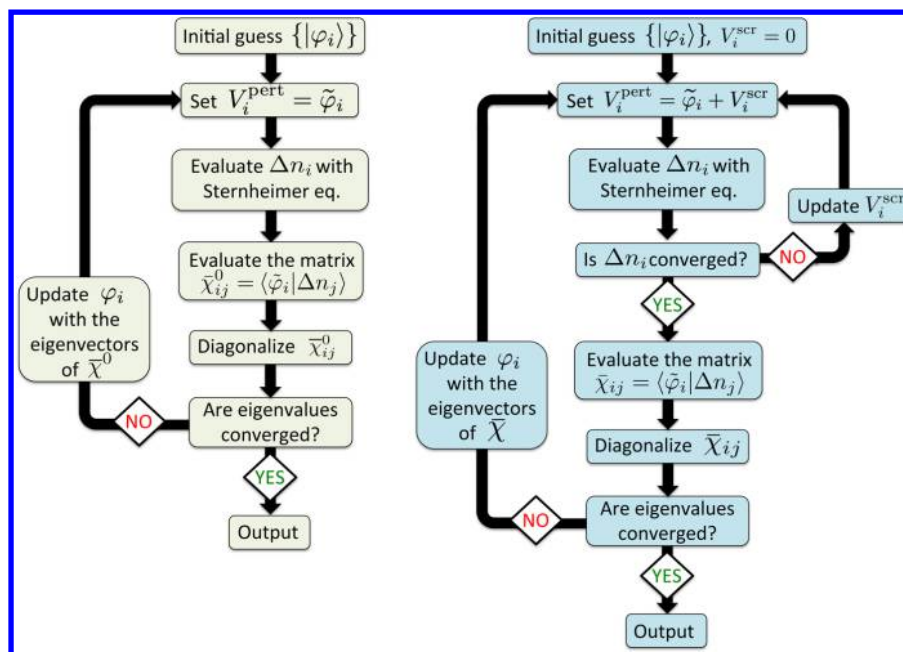


Figure 2. (Color online) Diagrams of the iterative diagonalization of the irreducible ($\bar{\chi}^0$, left panel) and reducible ($\bar{\chi}$, right panel) polarizability adopted in this work. In both cases, the initial set of vectors $\{|\varphi_i\rangle\}$ are assigned with random components. At each iteration the polarizability matrix is computed by evaluating the density response to the i -th perturbation using eq 44–46. The two diagrams differ only by the self-consistent inclusion of \hat{V}_i^{scr} in the solution of the Sternheimer equation.

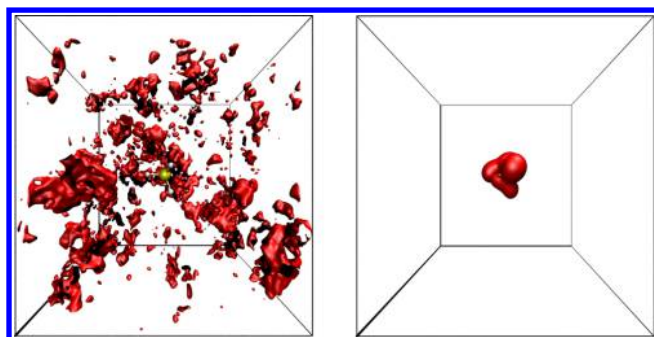


Figure 3. (Color online) Isosurfaces of the square modulus of the most screened eigenvector of the polarizability matrix of the silane molecule ($|\varphi_i(\mathbf{r})|^2$ in Figure 2, left panel). The iterative diagonalization was started from vectors with random components (left panel) and converges rapidly (3–4 iterations) to the potential shown in the right panel).

unperturbed system $|\psi_{n\mathbf{k}\sigma}\rangle$ may be evaluated using the Sternheimer equation:⁵⁴

$$(\hat{H}_{\text{KS}}^\sigma - \varepsilon_{n\mathbf{k}\sigma})\hat{P}_c^{\mathbf{k}\sigma}|\Delta\psi_{n\mathbf{k}\sigma}^i\rangle = -\hat{P}_c^{\mathbf{k}\sigma}\hat{V}_i^{\text{pert}}|\psi_{n\mathbf{k}\sigma}\rangle \quad (44)$$

Equation 44 may be iteratively solved using, for example, preconditioned conjugate-gradient methods. The linear variation of the density due to the i -th perturbation is obtained within density functional perturbation theory^{70,71} (DFPT) as

$$\Delta n_i(\mathbf{r}) = \sum_{\sigma} \sum_{n=1}^{N_{\text{occ}}^{\sigma}} \int_{\text{BZ}} \frac{d\mathbf{k}}{(2\pi)^3} [\psi_{n\mathbf{k}\sigma}^*(\mathbf{r})\Delta\psi_{n\mathbf{k}\sigma}^i(\mathbf{r}) + \text{c.c.}] \quad (45)$$

The matrix elements of the irreducible polarizability in the space spanned by φ_i are given by

$$\bar{\chi}_{ij}^0 = \langle \tilde{\varphi}_i | \Delta n_j \rangle \quad (46)$$

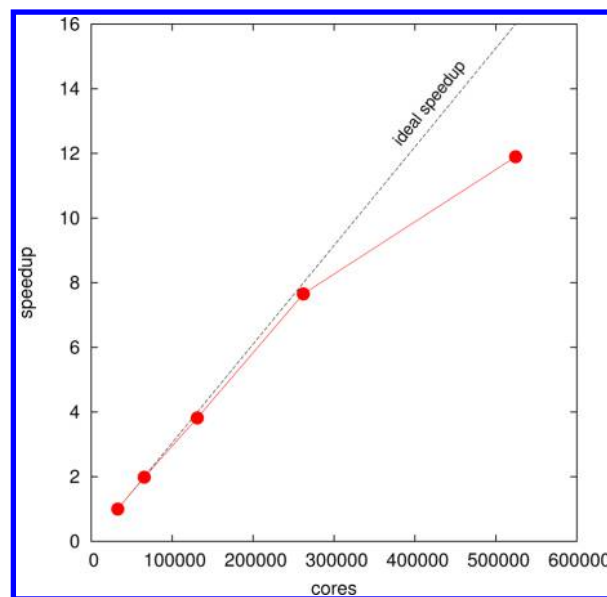


Figure 4. (Color online) Scalability of the PDEP iterative diagonalization (see Figure 2) of the static dielectric matrix of the COOH-Si/H₂O solid/liquid interface discussed in Section 4.2. The unit cell includes 492 atoms and 1560 valence electrons.

where $|\Delta n_i\rangle$ is computed using eqs 44 and 45 and assuming that $V_i^{\text{pert}}(\mathbf{G}) = \tilde{\varphi}_i(\mathbf{G})$. The matrix $\bar{\chi}_{ij}^0$ is then diagonalized to obtain new N_{pdep} basis vectors φ_i , and the procedure is iterated using, for example, a Davidson algorithm⁷² (See Figure 3). We note that at each iteration, all Sternheimer problems are independent from each other, thus offering the opportunity to carry out embarrassingly parallel calculations. A description of the parallel operations and data layout will be given elsewhere.⁷³ As a result, the algorithm shows a good scalability up to 524 288 cores (see Figure 4).

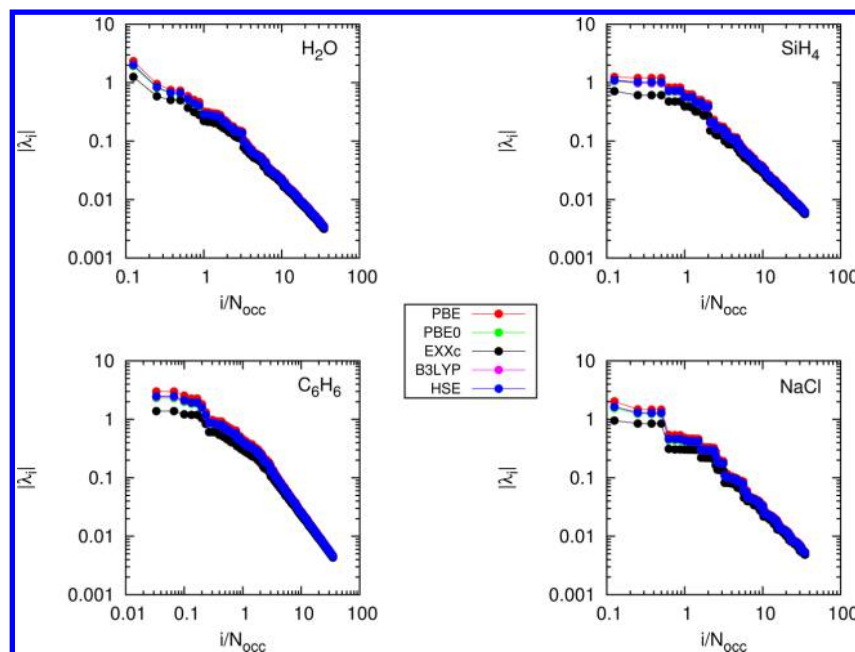


Figure 5. (Color online) Eigenvalues (λ_i) of the polarizability of H_2O , SiH_4 , C_6H_6 , and NaCl molecules, as obtained using the iterative diagonalization described in the left panel of Figure 2 (see text), and adopting five different exchange-correlation potentials for the KS Hamiltonian (see Table 2). N_{occ} is the number of valence bands.⁵²

As an example we show in Figure 5 the eigenvalues of the $\bar{\chi}_{ij}^0$ matrix obtained with the PDEP algorithm for the water, silane, benzene, and sodium chloride molecules, using KS Hamiltonians with different exchange-correlation functionals. The choice of the functional only affects the most screened eigenpotentials, whereas the eigenvalues λ_i corresponding to the least screened ones rapidly approach⁵¹ zero with a decay similar to that predicted by the Lindhard model.⁵² This indicates that the computation of the least screened eigenpotentials might be avoided and carried out using model functions.

If instead of $\bar{\chi}^0$, one wishes to diagonalize $\bar{\chi}$, the potential \hat{V}_i^{scr} arising from the rearrangements of the charge density in response to the applied perturbation needs to be included in the definition of the perturbation \hat{V}_i^{pert} of eq 44.^{61,74,75} In a generalized KS scheme, the \hat{V}_i^{scr} is given by

$$\hat{V}_i^{\text{scr}}|\psi_{n\mathbf{k}\sigma}\rangle = [\Delta\hat{V}_H^i + (1 - \alpha)\Delta\hat{V}_x^i + \Delta\hat{V}_c^i + \alpha\Delta\hat{V}_{\text{EXX}}^i]|\psi_{n\mathbf{k}\sigma}\rangle \quad (47)$$

where α is the fraction of exact exchange (EXX) that is admixed to the semilocal exchange potential. The linear variation of the Hartree potential is

$$\Delta\hat{V}_H^i|\psi_{n\mathbf{k}\sigma}\rangle = \int d\mathbf{r}' \Delta n_i(\mathbf{r}') \frac{e^2}{|\mathbf{r} - \mathbf{r}'|} \psi_{n\mathbf{k}\sigma}(\mathbf{r}) \quad (48)$$

and those of the exchange and correlation potentials are given by the functional derivatives:

$$\Delta\hat{V}_{x/c}^i|\psi_{n\mathbf{k}\sigma}\rangle = \frac{dV_{x/c}}{dn} \bigg|_{n(\mathbf{r})} \Delta n_i(\mathbf{r}) \psi_{n\mathbf{k}\sigma}(\mathbf{r}) \quad (49)$$

The linear variation of the exact exchange potential (EXX) is expressed in terms of variations of the single particle orbitals

$$\begin{aligned} \Delta\hat{V}_{\text{EXX}}^i|\psi_{n\mathbf{k}\sigma}\rangle = & - \sum_{m=1}^{N_{\text{occ}}} \int_{\text{BZ}} \frac{d\mathbf{k}'}{(2\pi)^3} \int d\mathbf{r}' [\Delta\psi_{m\mathbf{k}'\sigma}^{i*}(\mathbf{r}') \\ & \times \psi_{m\mathbf{k}'\sigma}(\mathbf{r}) + \psi_{m\mathbf{k}'\sigma}^*(\mathbf{r}') \Delta\psi_{m\mathbf{k}'\sigma}^i(\mathbf{r})] \frac{e^2}{|\mathbf{r} - \mathbf{r}'|} \psi_{n\mathbf{k}\sigma}(\mathbf{r}) \end{aligned} \quad (50)$$

We note that calculations including \hat{V}_i^{scr} require a double self-consistent procedure (see Figure 2); hence, it is computationally more efficient to iteratively diagonalize $\bar{\chi}^0$ first and then obtain the reducible polarizability $\bar{\chi}$ by linear algebra operations.⁷⁶ We recall that both $\bar{\chi}$ and $\bar{\chi}^0$ are Hermitian operators⁷⁷ and because of eq 18 they have the same eigenvectors.

2.4. Evaluation of G and W without Empty Electronic States Using a Lanczos Algorithm.

The calculation of the correlation self-energy, eqs 27–30, and of the screening, eqs 37–40, requires the computation of the matrix elements of $\hat{O}_{\text{KS}}^{\sigma}(\omega)$, defined in eq 25, for multiple values of ω . For each frequency ω , given two generic vectors $|L\rangle$ and $|R\rangle$, we define

$$M_{v;LR}^{\mathbf{k}\sigma}(\omega) = \langle L | \hat{P}_v^{\mathbf{k}\sigma} \hat{O}_{\text{KS}}^{\sigma}(\omega) \hat{P}_v^{\mathbf{k}\sigma} | R \rangle \quad (51)$$

and

$$M_{c;LR}^{\mathbf{k}\sigma}(\omega) = \langle L | \hat{P}_c^{\mathbf{k}\sigma} \hat{O}_{\text{KS}}^{\sigma}(\omega) \hat{P}_c^{\mathbf{k}\sigma} | R \rangle \quad (52)$$

Equation 51 can be easily written in terms of the eigenstates $\psi_{n\mathbf{k}\sigma}$ and eigenvalues $\varepsilon_{n\mathbf{k}\sigma}$ of the KS Hamiltonian:

$$M_{v;LR}^{\mathbf{k}\sigma}(\omega) = - \sum_{n=1}^{N_{\text{occ}}} \frac{\langle L | \psi_{n\mathbf{k}\sigma} \rangle \langle \psi_{n\mathbf{k}\sigma} | R \rangle}{\varepsilon_{n\mathbf{k}\sigma} - \omega} \quad (53)$$

Equation 52 may be cast as well in terms of the occupied states and energies, by using the relation $\hat{P}_c^{\mathbf{k}\sigma} = 1 - \hat{P}_v^{\mathbf{k}\sigma}$ and writing $\tilde{H}_{\text{KS}}^{\sigma} = \hat{P}_c^{\mathbf{k}\sigma} \hat{H}_{\text{KS}}^{\sigma} \hat{P}_c^{\mathbf{k}\sigma}$ (called deflated Hamiltonian)

$$M_{c;LR}^{\mathbf{k}\sigma}(\omega) = - \langle L | \hat{P}_c^{\mathbf{k}\sigma} (\tilde{H}_{\text{KS}}^{\sigma} - \omega)^{-1} \hat{P}_c^{\mathbf{k}\sigma} | R \rangle \quad (54)$$

The Lanczos algorithm⁷⁸ is used to obtain a set of N_{lanczos} orthonormal vectors $Q = \{|q_n\rangle; n = 1, N_{\text{lanczos}}\}$ that are used to recast the deflated Hamiltonian in eq 54 into a tridiagonal form:

$$T = Q^\dagger \tilde{H}_{\text{KS}}^\sigma Q = \begin{pmatrix} \alpha_1 & \beta_2 & & \\ \beta_2 & \alpha_2 & \beta_3 & \\ & \beta_3 & \ddots & \ddots \\ & & \ddots & \ddots & \beta_n \\ & & & \beta_n & \alpha_n \end{pmatrix} \quad (55)$$

where

$$\alpha_n = \langle q_n | \tilde{H}_{\text{KS}}^\sigma | q_n \rangle \quad (56)$$

$$\beta_{n+1} = \|(\tilde{H}_{\text{KS}}^\sigma - \alpha_n)|q_n\rangle - \beta_n|q_{n-1}\rangle\| \quad (57)$$

The calculation of the sequence of vectors $|q_n\rangle$, called Lanczos chain, is started by imposing $|q_1\rangle = \hat{P}_c^{\text{KS}}|R\rangle$; iterations are performed⁷⁹ by enforcing orthogonality through the recursive relation:

$$|q_{n+1}\rangle = \frac{1}{\beta_{n+1}}[(\tilde{H}_{\text{KS}}^\sigma - \alpha_n)|q_n\rangle - \beta_n|q_{n-1}\rangle] \quad (58)$$

The tridiagonal matrix T can be diagonalized using an orthogonal transformation U , so that $D = U^T T U$. Using d_n to indicate the n -th element of the diagonal matrix D , we obtain

$$M_{c;LR}^{\text{KS}}(\omega) = - \sum_{n_1, n_2, n_3=1}^{N_{\text{lanczos}}} \langle L | q_{n_1} \rangle U_{n_1 n_2} \frac{1}{d_{n_2} - \omega} U_{n_3 n_2} \langle q_{n_3} | R \rangle \quad (59)$$

Because of the orthogonality of the elements belonging to a Lanczos chain, we have $\langle q_{n_3} | R \rangle = \delta_{n_3,1}$, yielding

$$M_{c;LR}^{\text{KS}}(\omega) = - \sum_{n_1, n_2=1}^{N_{\text{lanczos}}} \langle L | q_{n_1} \rangle U_{n_1 n_2} \frac{1}{d_{n_2} - \omega} U_{1 n_2} \quad (60)$$

Equation 60 is written in a form similar to eq 53, where the coefficients of the expansion are independent of the value of ω and therefore it is not necessary to recompute them for multiple frequencies. However, the coefficients of the expansion in eq 60 depend by construction on the vector $|R\rangle$ that is used to start the Lanczos chain. Therefore, to evaluate $M_{c;LR}^{\text{KS}}(\omega)$ one needs to solve as many Lanczos problems as the number of vectors $|R\rangle$, while the eigendecomposition used for $M_{v;LR}^{\text{KS}}(\omega)$ in eq 53 is unique. Because Lanczos chains are independent of each other, the iterations can be performed in an embarrassingly parallel fashion, similarly to the procedure discussed in Section 2.3 for the computation of the PDEP basis set.

In our calculations, we used eq 53, with an explicit summation over occupied eigenstates, for the evaluation of the terms in eq 27 and eq 29, whereas we used the Lanczos expansion of eq 60 to evaluate the terms in eqs 28, 30, and 37–40.

2.5. Contour Deformation Technique. In eqs 26–30 the frequency integration may be carried out by using complex analysis, and thus avoiding the integration in the real frequency domain. A closed integration contour on the complex plane is identified for which Cauchy's theorem and Jordan's Lemma apply.⁸⁰ This approach is called contour deformation technique^{29,81} and establishes a formal identity between the

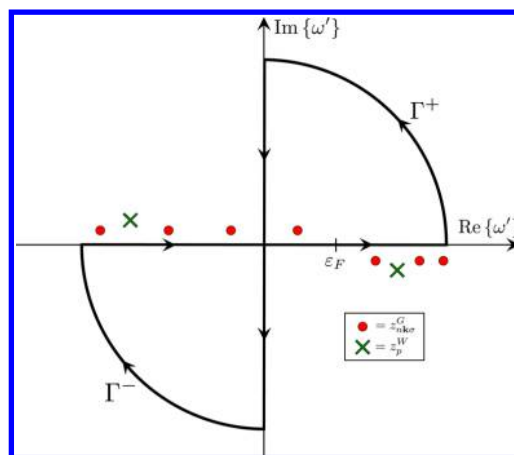


Figure 6. (Color online) Contours used in this work (see text). The integration contours Γ^+ and Γ^- enclose only the poles of the Green's function $z_{nk\sigma}^G$ (dots) and exclude the poles of the screened Coulomb interaction z_p^W (crosses).

Table 2. Exchange and Correlation Potentials Used in This Work (See Text)^a

functional	semilocal exchange	nonlocal exchange	correlation
PBE ^b	$V_x^{\text{PBE}}(\mathbf{r})$	—	$V_c^{\text{PBE}}(\mathbf{r})$
PBE0 ^c	$0.75 V_x^{\text{PBE}}(\mathbf{r})$	$0.25 V_x^{\text{EXX}}(\mathbf{r}, \mathbf{r}')$	$V_c^{\text{PBE}}(\mathbf{r})$
EXXC ^d		$V_x^{\text{EXX}}(\mathbf{r}, \mathbf{r}')$	$V_c^{\text{PBE}}(\mathbf{r})$
B3LYP ^e	$0.08 V_x^{\text{LDA}}(\mathbf{r}) + 0.72 V_x^{\text{GGA}}(\mathbf{r})$	$0.2 V_x^{\text{EXX}}(\mathbf{r}, \mathbf{r}')$	$0.19 V_c^{\text{LDA}}(\mathbf{r}) + 0.81 V_c^{\text{GGA}}(\mathbf{r})$
HSE ^f	$0.75 V_x^{\text{PBE,SR}}(\mathbf{r}; \mu) + V_x^{\text{PBE,LR}}(\mathbf{r}; \mu)$	$0.25 V_x^{\text{EXX,SR}}(\mathbf{r}, \mathbf{r}'; \mu)$	$V_c^{\text{PBE}}(\mathbf{r})$

^aFor HSE, the screening parameter $\mu = 0.106 \text{ bohr}^{-1}$ divides the exchange (x) contributions into short range (SR) and long range (LR).¹⁰¹ ^bRef 102. ^cRef 103. ^dRef 104. ^eRef 105. ^fRef 101.

quantities reported in eq 26 and an equivalent set of quantities that are numerically more stable to compute. The poles of the Green's function $G_{\text{KS}}^\sigma(\mathbf{r}, \mathbf{r}'; \omega + \omega')$ are located at complex frequencies $z_{nk\sigma}^G$ satisfying the relation

$$z_{nk\sigma}^G = \epsilon_{nk\sigma} - \omega - i\eta \text{sign}(\epsilon_{nk\sigma} - \epsilon_F) \quad (61)$$

with a numerical residue given by

$$\text{Res}\{G_{\text{KS}}^\sigma(\mathbf{r}, \mathbf{r}'), z_{nk\sigma}^G\} = \psi_{nk\sigma}(\mathbf{r}) \psi_{nk\sigma}^*(\mathbf{r}') \quad (62)$$

The poles of W_p correspond to the plasmon energies of the system: $z_p^W = \pm (\Omega_p - i\eta)$. The matrix elements of the correlation self-energy can be computed by using the integration contour shown in Figure 6, yielding:

$$\begin{aligned} \Sigma_c^\sigma(\mathbf{r}, \mathbf{r}'; \omega) = & i \int_{-\infty}^{+\infty} \frac{d\omega'}{2\pi} G_{\text{KS}}^\sigma(\mathbf{r}, \mathbf{r}'; \omega + \omega') W_p(\mathbf{r}, \mathbf{r}'; \omega') \\ & - \sum_{z_{nk\sigma}^G \in \Gamma^+} \psi_{nk\sigma}(\mathbf{r}) \psi_{nk\sigma}^*(\mathbf{r}') W_p(\mathbf{r}, \mathbf{r}'; z_{nk\sigma}^G) \\ & + \sum_{z_{nk\sigma}^G \in \Gamma^-} \psi_{nk\sigma}(\mathbf{r}) \psi_{nk\sigma}^*(\mathbf{r}') W_p(\mathbf{r}, \mathbf{r}'; z_{nk\sigma}^G) \end{aligned} \quad (63)$$

In view of the chosen contour, as the frequency ω is varied, the poles of W_p never fall inside the two closed contours Γ^+ and Γ^- , which therefore may only enclose poles of the Green's function. The correlation self-energy is thus obtained as the sum of (i) an integral along the imaginary axis, where both G_{KS}^σ and W_{RPA} are smooth functions, and (ii) all the numerical

Table 3. Vertical Ionization Potential (VIP, eV) of Closed Shell Molecules^a

molecule	G ₀ W ₀ (PBE)	G ₀ W ₀ (PBE0)	G ₀ W ₀ (EXXc)	G ₀ W ₀ (B3LYP)	G ₀ W ₀ (HSE)	exp.
C ₂ H ₂	11.10 (7.20)	11.38 (8.43)	11.66 (12.19)	11.37 (8.45)	11.30 (8.03)	11.49
C ₂ H ₄	10.35 (6.74)	10.56 (7.86)	10.74 (11.26)	10.58 (7.88)	10.50 (7.46)	10.68
C ₄ H ₄ S	8.90 (5.98)	9.15 (7.01)	9.44 (10.12)	9.16 (7.05)	9.08 (6.62)	8.86
C ₆ H ₆	9.10 (6.33)	9.32 (7.30)	9.54 (10.21)	9.34 (7.33)	9.25 (6.91)	9.25
CH ₃ Cl	11.27 (7.10)	11.57 (8.50)	11.89 (12.81)	11.56 (8.57)	11.49 (8.11)	11.29
CH ₃ OH	10.47 (6.24)	10.93 (7.91)	11.52 (13.05)	10.86 (8.01)	10.82 (7.51)	10.96
CH ₃ SH	9.31 (5.55)	9.57 (6.78)	9.83 (10.58)	9.59 (6.87)	9.49 (6.39)	9.44
CH ₄	13.99 (9.46)	14.34 (10.99)	14.78 (15.71)	14.34 (11.08)	14.26 (10.60)	14.40
Cl ₂	11.48 (7.28)	11.78 (8.69)	12.14 (13.02)	11.77 (8.77)	11.70 (8.29)	11.49
ClF	12.47 (7.83)	12.84 (9.44)	13.35 (14.33)	12.83 (9.53)	12.76 (8.04)	12.77
CO	13.45 (9.06)	14.01 (10.74)	14.88 (15.91)	13.99 (10.88)	13.91 (10.34)	14.01
CO ₂	13.31 (9.08)	13.73 (10.69)	14.34 (15.77)	13.65 (10.76)	13.64 (10.29)	13.78
CS	10.92 (7.38)	11.53 (8.89)	12.51 (13.55)	11.49 (9.02)	11.40 (8.49)	11.33 ^b
F ₂	14.90 (9.42)	15.51 (11.73)	16.34 (18.87)	15.42 (11.82)	15.40 (11.33)	15.70
H ₂ CO	10.38 (6.25)	10.85 (7.84)	11.43 (12.82)	10.78 (7.97)	10.74 (7.44)	10.89
H ₂ O	11.81 (7.23)	12.37 (9.04)	12.91 (14.67)	12.31 (9.12)	12.24 (8.63)	12.62 ^b
H ₂ O ₂	10.96 (6.43)	11.47 (8.29)	12.13 (14.06)	11.40 (8.40)	11.36 (7.88)	11.70
HCl	12.54 (8.03)	12.84 (9.48)	13.12 (13.93)	12.85 (9.54)	12.76 (9.08)	12.74 ^b
HCN	13.30 (9.02)	13.63 (10.39)	13.96 (14.54)	13.60 (10.40)	13.55 (9.99)	13.71
HF	15.14 (9.64)	15.72 (11.80)	16.28 (18.52)	15.65 (11.86)	15.60 (11.39)	16.12
HOCl	10.93 (6.61)	11.32 (8.18)	11.84 (12.97)	11.28 (8.29)	11.23 (7.79)	11.12 ^b
Li ₂	5.03 (3.23)	5.29 (3.80)	5.39 (5.55)	5.29 (3.87)	5.14 (3.43)	5.11 ^b
LiF	9.97 (6.07)	10.85 (7.88)	11.45 (13.74)	10.79 (7.95)	10.66 (7.47)	11.30 ^b
LiH	6.58 (4.35)	7.57 (5.42)	8.29 (8.86)	7.51 (5.53)	7.26 (5.02)	7.90 ^b
N ₂	14.95 (10.29)	15.54 (12.20)	17.23 (17.80)	15.48 (12.34)	15.43 (11.80)	15.58
N ₂ H ₄	9.28 (5.28)	9.72 (6.80)	10.24 (11.55)	9.68 (6.92)	9.62 (6.40)	8.98
Na ₂	4.73 (3.13)	4.86 (3.60)	4.88 (5.04)	4.89 (3.72)	4.78 (3.24)	4.89 ^b
NaCl	8.30 (5.23)	9.12 (6.48)	9.49 (10.47)	9.09 (6.53)	8.93 (6.08)	9.80
NH ₃	10.20 (6.16)	10.72 (7.71)	11.26 (12.55)	10.68 (7.80)	10.59 (7.31)	10.82
P ₂	10.44 (7.11)	10.62 (8.09)	10.76 (11.06)	10.63 (8.12)	10.56 (7.70)	10.62
PH ₃	10.46 (6.73)	10.70 (7.88)	10.94 (11.45)	10.73 (7.99)	10.63 (7.49)	10.59
SH ₂	10.26 (6.29)	10.53 (7.55)	10.76 (11.40)	10.55 (7.62)	10.45 (7.15)	10.50
Si ₂ H ₆	10.45 (7.18)	10.71 (8.28)	11.06 (11.75)	10.78 (8.40)	10.64 (7.90)	10.53
SiH ₄	12.44 (8.52)	12.82 (9.86)	13.32 (14.03)	12.83 (9.97)	12.72 (9.46)	12.30
SiO	11.09 (7.49)	11.51 (8.84)	12.10 (12.75)	11.47 (8.94)	11.41 (8.44)	11.49
SO ₂	11.96 (8.08)	12.44 (9.61)	13.15 (14.39)	12.39 (9.75)	12.34 (9.22)	12.50
ME (eV)	−0.42 (−4.29)	0.00 (−2.87)	0.49 (1.50)	−0.02 (−2.78)	−0.10 (−3.27)	
MAE (eV)	0.44 (4.29)	0.19 (2.87)	0.51 (1.50)	0.21 (2.78)	0.22 (3.27)	
MRE(%)	−3.68 (−37.98)	0.15 (−25.51)	4.31 (13.00)	−0.02 (−24.70)	−0.86 (−29.22)	
MARE(%)	3.96 (37.98)	1.78 (25.51)	4.49 (13.00)	1.96 (24.70)	2.03 (29.22)	

^aExperimental values are taken from the NIST computational chemistry database.⁹⁷ Each column reports the VIP obtained with the West code by performing G₀W₀ calculations starting from the solutions of the Kohn-Sham equations with the exchange and correlation potential (see Table 2), specified within parentheses on the first row. In parentheses we report the absolute value of the HOMO energy prior to the application of G₀W₀ corrections. ME, MAE, MRE, and MARE stand for mean, mean absolute, mean relative, and mean relative absolute error as compared to the experiment, respectively. ^bThe NIST computational chemistry database⁹⁷ does not report the VIP but the ionization potential.

residues arising from G_{KS}^{σ} , shifted inside the integration contours, depending on the value of ω . The matrix element of the correlation self-energy becomes

$$\begin{aligned}
 & \langle \psi_{n\mathbf{k}\sigma} | \Sigma_{\text{C}}^{\sigma}(E_{n\mathbf{k}\sigma}^{\text{QP}}) | \psi_{n\mathbf{k}\sigma} \rangle \\
 &= - \int_{-\infty}^{+\infty} \frac{d\omega'}{2\pi} \langle \psi_{n\mathbf{k}\sigma} | G_{\text{KS}}^{\sigma}(\mathbf{r}, \mathbf{r}'; E_{n\mathbf{k}\sigma}^{\text{QP}} + i\omega') \\
 & \quad \times W_{\text{p}}(\mathbf{r}, \mathbf{r}'; i\omega') | \psi_{n\mathbf{k}\sigma} \rangle + \sum_m f_{m\mathbf{k}\sigma}^{\text{nk}\sigma} \langle \psi_{n\mathbf{k}\sigma} | \psi_{m\mathbf{k}\sigma}(\mathbf{r}) \\
 & \quad \times W_{\text{p}}(\mathbf{r}, \mathbf{r}'; \epsilon_{m\mathbf{k}\sigma} - E_{n\mathbf{k}\sigma}^{\text{QP}}) \psi_{m\mathbf{k}\sigma}^*(\mathbf{r}') | \psi_{n\mathbf{k}\sigma} \rangle \quad (64)
 \end{aligned}$$

where the function $f_{m\mathbf{k}\sigma}^{\text{nk}\sigma}$ is

$$f_{m\mathbf{k}\sigma}^{\text{nk}\sigma} = \begin{cases} +1 & \text{if } \epsilon_{\text{F}} < \epsilon_{m\mathbf{k}\sigma} < E_{n\mathbf{k}\sigma}^{\text{QP}} \\ -1 & \text{if } E_{n\mathbf{k}\sigma}^{\text{QP}} < \epsilon_{m\mathbf{k}\sigma} < \epsilon_{\text{F}} \\ 0 & \text{otherwise} \end{cases} \quad (65)$$

Equation 65 shows that only a finite number of residues needs to be computed.⁸² Inserting eq 22 for W_{p} into eq 64, eqs 26–30 are solved. The integration over the imaginary axis is performed numerically by considering a nonuniform grid, finer for small frequencies. With the introduction of the contour deformation technique we avoid the use of plasmon pole models^{28,47,83–86} to describe the frequency dependence of the screening and we overcome the limitations of the analytic continuation^{87,88} reported in refs 39 and 40.

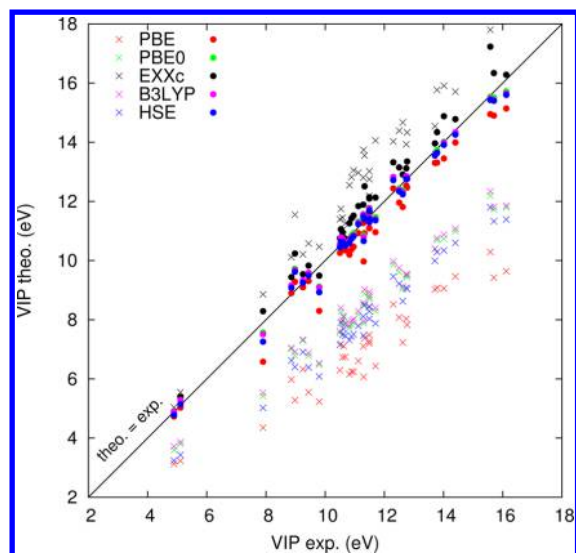


Figure 7. (Color online) Comparison between calculated and experimental vertical ionization potential (VIP) for the set of 36 closed-shell molecules listed in Table 3. Dots (crosses) refer to VIPs obtained at the G_0W_0 (DFT) level of theory.

3. VERIFICATION AND VALIDATION OF RESULTS

In this section we present several results obtained with the G_0W_0 method presented in Section 2. In particular we computed the vertical ionization potential (VIP) of closed and open-shell molecules and the electronic structure of several crystalline, amorphous and liquid systems. All results were obtained by computing KS eigenvalues and eigenvectors with the QuantumEspresso package⁸⁹ and the G_0W_0 quasiparticle energies with the West code, which features a parallel implementation of the method of Section 2.

3.1. Vertical Ionization Potentials of Molecules. We considered a subset of the G2/97 test set⁹⁰ composed of 36 closed shell molecules, listed in Table 3. Subsets of the G2/97 set were recently used to benchmark G_0W_0 calculations with both localized^{91–95} and plane wave^{40,96} basis sets. Molecular geometries were taken from the NIST computational chemistry database,⁹⁷ and no additional structural relaxations were performed. In our calculations, each molecule was placed in a periodically repeated cell of edge 30 bohr; the interaction between ionic cores and valence electrons was described by a PBE norm conserving pseudopotential; we used a plane wave basis set with a kinetic energy cutoff of 85 Ry (chosen so as to be appropriate for the hardest pseudopotential, i.e., those of oxygen and fluorine). At the DFT-KS level of theory, we approximated the VIP by the absolute value of the highest occupied KS eigenvalue (HOMO)⁹⁸ and we considered five different exchange and correlation functionals: PBE, PBE0, EXXc, B3LYP, and HSE, whose expressions are summarized in Table 2. The computed DFT-KS VIP are reported in Table 3 within parentheses and in Figure 7 as crosses. As expected, hybrid functionals yielded a better agreement with experiments than PBE: the mean absolute relative errors (MARE) are 13.00%, 24.70%, 25.51%, and 29.22% for EXXc, B3LYP, PBE0, and HSE respectively, whereas the MARE of PBE is substantially higher, 37.98%.

Corrections to the DFT eigenvalues were computed within the G_0W_0 approximation using the five different starting points obtained with the various functionals. The PDEP basis set of each system was generated including a number of eigenpotentials N_{pdep} proportional to the number of valence electrons, for instance $N_{\text{pdep}} = 1050$ for the largest molecule considered here (i.e., C_6H_6). The G_0W_0 corrected VIPs are reported in Table 3 and in Figure 7 as dots; we obtained values in much better agreement with experiments, with MARE of 1.78%, 1.96%,

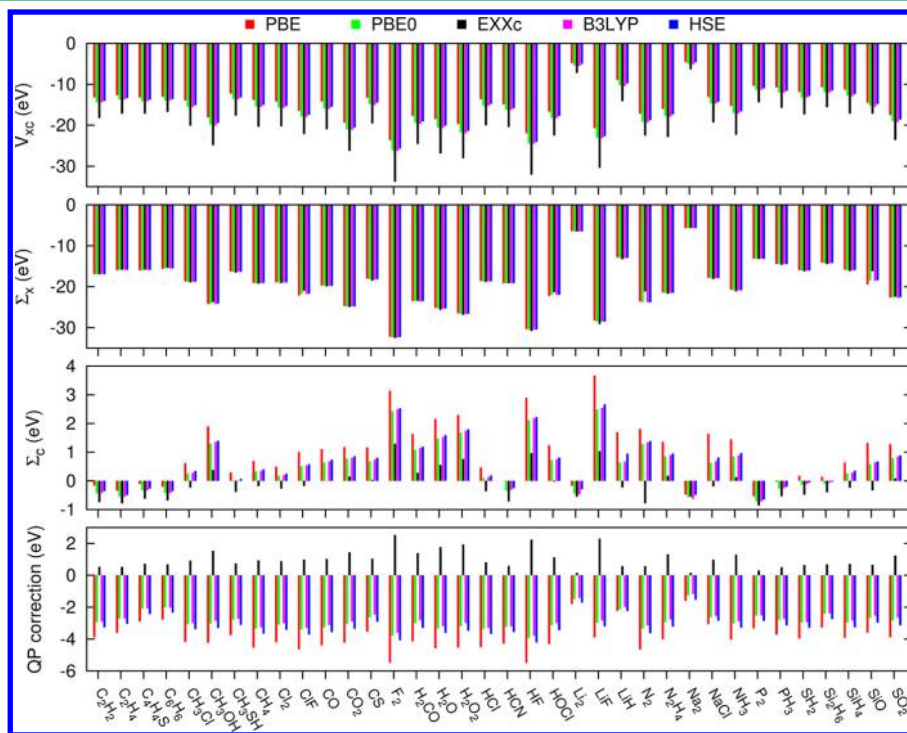


Figure 8. (Color online) The matrix elements of $V_{x\sigma}$, $\Sigma_{x\sigma}$ and Σ_c ($E_{nk\sigma}^{\text{QP}}$) evaluated on the HOMO eigenstate, for different choices of the exchange and correlation potential (see Table 2). The bottom panel reports the QP correction, that is, the difference $E_{nk\sigma}^{\text{QP}} - \epsilon_{nk\sigma}$ (see eqs 5, 9, and 10).

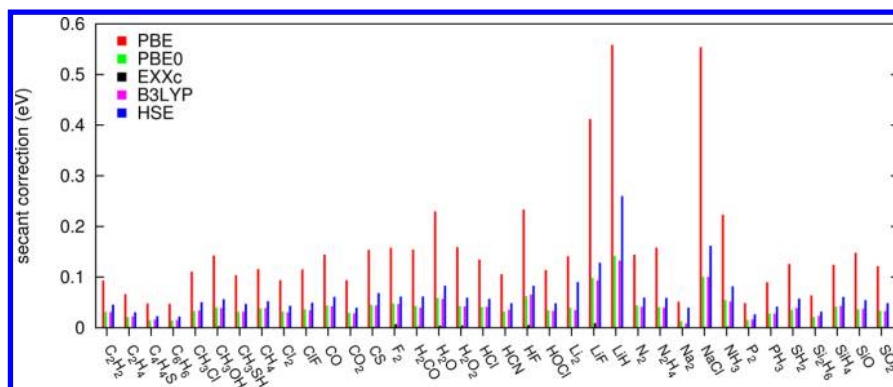


Figure 9. (Color online) Difference between the solution of eq 5 using a secant algorithm and employing the first order Taylor expansion of eq 66.

Table 4. Vertical Ionization Potential (VIP, eV) of Open Shell Molecules^a

molecule	spin	G_0W_0 (LDA)	G_0W_0 (PBE)	exp.
CF	0.5	8.92 (4.68)	8.69 (4.72)	9.55
NF	1.0	12.18 (7.14)	11.81 (7.05)	12.63
NO ₂	0.5	10.82 (6.63)	10.46 (6.55)	11.23
O ₂	1.0	12.11 (6.92)	11.67 (6.87)	12.33
S ₂	1.0	9.53 (5.86)	9.34 (5.82)	9.55

^aExperimental values are taken from the NIST computational chemistry database.⁹⁷ Each column reports the VIP obtained with the West code by performing G_0W_0 calculations starting from the solutions of the Kohn-Sham equations with the exchange and correlation potential (LDA or PBE), specified within parentheses on the first row. In parentheses we report the absolute value of the HOMO energy prior to the application of G_0W_0 corrections.

2.03%, 3.96%, and 4.49% for PBE0, B3LYP, HSE, PBE, and EXXc starting points, respectively. We note that the QP corrections to HOMO DFT eigenvalues have different signs, depending on the starting point: the corrections lead to a decrease of the VIPs obtained with EXXc but to an increase of

those computed with the other functionals. In Figure 8, we analyzed separately the matrix elements of V_{xc} , Σ_X and Σ_C (see eq 5); the latter is the most affected by the choice of the exchange correlation functional at the DFT level. The matrix elements of Σ_X are instead weakly affected by the choice of the starting point.

In many papers in the literature,^{93,95} eq 5 is solved using a linear approximation:⁴⁷

$$E_{nk\sigma}^{\text{QP}} \approx \epsilon_{nk\sigma} + Z_{nk\sigma} [\langle \psi_{nk\sigma} | \hat{\Sigma}^{\sigma}(\epsilon_{nk\sigma}) | \psi_{nk\sigma} \rangle - \langle \psi_{nk\sigma} | \hat{V}_{xc}^{\sigma} | \psi_{nk\sigma} \rangle] \quad (66)$$

where $Z_{nk\sigma}^{-1} = 1 - (\partial/\partial\omega) \langle \psi_{nk\sigma} | \hat{\Sigma}^{\sigma}(\omega) | \psi_{nk\sigma} \rangle |_{\omega=\epsilon_{nk\sigma}}$. Here, we employed instead a secant method to find the roots of eq 5, where eq 66 was used to determine the starting point of the iterative procedure. The difference between VIPs obtained with eq 66 and using the secant method varies within 0–0.5 eV; see Figure 9.

We also considered five open shell molecules, including the O₂ molecule in its triplet ground state. The VIPs computed at the DFT level using LDA or the PBE exchange-correlation functional⁹⁹ and by computing the QP corrections with G_0W_0

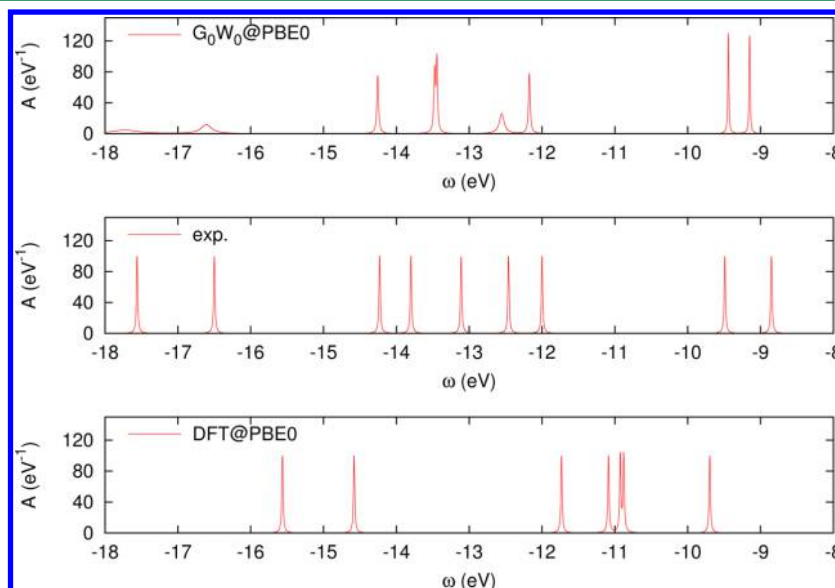


Figure 10. (Color online) The spectral function $A(\omega)$ (see text) for the thiophene molecule (C_4H_4S). The peaks reported in the middle panel are located at the measured ionization potentials.¹⁰⁶ The top (bottom) panel shows the spectral functions obtained at the G_0W_0 (DFT) level of theory, using the PBE0 exchange and correlation potential. The width of the peaks is set equal to 0.01 eV, except for the top panel where electronic lifetimes are computed as imaginary part of the self-energies.

Table 5. Quasiparticle (QP) Energies of Si at High Symmetry Points, Compared with Previous Calculations and Experiment

k-point	G_0W_0 (LDA)	G_0W_0 (PBE)	theor.	exp.
L_{1c}	2.26 (1.47)	2.29 (1.59)	2.21 ^a , 2.14 ^c , 2.18 ^d , 2.13 ^e , 2.19 ^f , 2.05 ^g	2.1 ^j , 2.4 ± 0.1 ^k
L'_{3v}	−1.25 (−1.20)	−1.21 (−1.20)	−1.23 ^a , −1.17 ^c , −1.20 ^d , −1.25 ^e , −1.25 ^f , −1.16 ^g	−1.2 ± 0.2 ^h
Γ_{15c}	3.35 (2.54)	3.32 (2.55)	3.25 ^a , 3.24 ^b , 3.24 ^c , 3.23 ^d , 3.25 ^e , 3.36 ^f , 3.09 ^g	3.40 ^h , 3.05 ⁱ
Γ'_{15v}	0.0 (0.0)	0.0 (0.0)	0.0	0.0
X_{1c}	1.44 (0.63)	1.37 (0.72)	1.36 ^a , 1.41 ^b , 1.34 ^c , 1.35 ^d , 1.31 ^e , 1.43 ^f , 1.01 ^g	1.3 ^h , 1.25 ⁱ
X_{4v}	−2.92 (−2.87)	−2.96 (−2.85)	−2.88 ^a , −2.80 ^b , −2.80 ^c , −2.83 ^d , −2.96 ^e , −2.93 ^f , −2.90 ^g	−2.90 ^h , −3.3 ± 0.2 ^m

^aRef 40. ^bRef 55. ^cRef 87. ^dRef 109. ^eRef 104. ^fRef 110. ^gRef 111. ^hRef 112. ⁱRef 113. ^jRef 114. ^kRef 115. ^lRef 116. ^mRef 117.

are summarized in Table 4. The G_0W_0 results are in satisfactory agreement with the experimental data,⁹⁷ and for the systems considered here, LDA seems to provide a better starting point for G_0W_0 than PBE.

We conclude this section dedicated to the validation of the West code for molecular systems by showing that G_0W_0 corrections may also improve higher order VIPs, that is, vertical ionization energies obtained by removing electrons from single particle states deeper in energy than the HOMO. As an example, we chose the thiophene (C_4H_4S) molecule whose spectral function $A(\omega) = |(1/\pi)\text{Tr}\{\text{Im}G_0(\omega)\}|$ was computed within G_0W_0 , starting from DFT energies obtained using the PBE0 functional (see Figure 10). We found that G_0W_0 gives a much improved description of higher order VIPs with respect to KS-DFT. While for the experimental and the PBE0 spectral functions we used an artificial smearing parameter of $\eta = 0.01$ eV to simulate finite lifetimes, in the case of the G_0W_0 spectral function, the electronic lifetimes were computed from first-principles, as the imaginary part of the electron self-energy. Our results are in good agreement with those reported by F. Caruso et al.¹⁰⁰ using localized basis sets.

3.2. Electronic Structure of Crystalline, Amorphous, and Aqueous Systems. We considered three crystalline systems Si, SiC, and AlAs, one amorphous Si_3N_4 , and one liquid water snapshot. The KS electronic structure was computed using super cells and the Γ point: 64 atoms and 256 valence electrons for Si, SiC, and AlAs, with cell edges of 20.53, 16.48, and 21.34 bohr, respectively; the amorphous Si_3N_4 sample consisted of 56 atoms and 256 electrons. For Si, SiC, AlAs and amorphous Si_3N_4 we used a kinetic energy cutoff of 60 Ry. The snapshot of 64 water molecules is taken from a 20 ps trajectory of a Born–Oppenheimer ab initio molecular dynamics simulation of liquid water (see ref 41); and it was described with a cutoff of 85 Ry. In our G_0W_0 calculations for condensed systems, we used $N_{\text{pdep}} = 1024$.

The QP energies of the crystalline solids at high symmetry k-points are reported in Tables 5, 6, and 7, where KS energies are given within brackets. The results obtained with West compare well with those of other plane wave pseudopotential calculations and with experiments.

The QP corrections of amorphous Si_3N_4 and liquid water are reported in Figure 11, where again we found that the West results compare well with those of existing calculations^{41,107} and experiments.¹⁰⁸

4. LARGE SCALE CALCULATIONS

The method discussed in Section 2, implemented in the West code and validated in Section 3 may be used to perform highly parallel G_0W_0 calculations and tackle large systems, with >1000 of valence electrons in the unit cell. We discuss the performance of the method for both finite and periodic systems, in

Table 6. Quasiparticle (QP) Energies of SiC at High Symmetry Points, Compared with Previous Calculations and Experiment

k-point	G_0W_0 (LDA)	G_0W_0 (PBE)	theor.	exp.
L_{1c}	6.46 (5.15)	6.37 (5.19)	6.43 ^a , 6.30 ^b , 6.45 ^c	6.35 ^d
L_{3v}	−1.18 (−1.09)	−1.16 (−1.06)	−1.10 ^a , −1.21 ^b	−1.15 ^d
Γ_{1c}	7.42 (6.29)	7.52 (6.29)	7.26 ^a , 7.19 ^b , 7.23 ^c	7.4 ^e
Γ'_{15v}	0.0 (0.0)	0.0 (0.0)	0.0	0.0
X_{1c}	2.45 (1.29)	2.28 (1.35)	2.31 ^a , 2.19 ^b , 1.80 ^c	2.39 ^d , 2.42 ^d
X_{5v}	−3.46 (−3.25)	−3.46 (−3.19)	−3.47 ^a , −3.53 ^b	−3.6 ^d

^aRef 40. ^bRef 109. ^cRef 111. ^dRef 112. ^eRef 118.

Table 7. Quasiparticle (QP) Energies of AlAs at High Symmetry Points, Compared with Previous Calculations and Experiment

k-point	G_0W_0 (LDA)	G_0W_0 (PBE)	theor.	exp.
L_{1c}	3.08 (2.15)	2.94 (2.15)	3.02 ^c , 2.84 ^a , 2.99 ^b	2.36 ^d
L_{3v}	−0.86 (−0.80)	−0.90 (−0.84)	−0.9 ^e , −0.87 ^a	
Γ_{1c}	3.15 (2.20)	2.99 (2.23)	2.96 ^e , 2.74 ^a , 2.72 ^b	3.13 ^c
Γ'_{15v}	0.0 (0.0)	0.0 (0.0)	0.0	0.0
X_{1c}	2.20 (1.35)	2.01 (1.37)	2.13 ^e , 2.16 ^a , 1.57 ^b	2.23 ^c
X_{5v}	−2.25 (−2.15)	−2.35 (−2.21)	−2.20 ^e , −2.27 ^a	−2.41 ^c

^aRef 40. ^bRef 109. ^cRef 111. ^dRef 112. ^eRef 119.

particular for Si nanocrystals and interfaces of functionalized Si surfaces and water, with up to 1344 and 1560 valence electrons in the unit cell, respectively.

4.1. Silicon Nanocrystals. We considered four Si-NCs: $Si_{35}H_{36}$ (1.3 nm), $Si_{87}H_{76}$ (1.6 nm), $Si_{147}H_{100}$ (1.9 nm), and $Si_{293}H_{172}$ (2.4 nm).¹²⁰ The structure of each NCs was obtained by carving out of bulk Si a sphere of Si atoms of given radius, by terminating all dangling bonds with H atoms and by relaxing the NC structure within DFT-PBE. A kinetic energy cutoff of 25 Ry, PBE norm-conserving pseudopotentials and a cubic cell of edge 90 bohr were used. The computed HOMO and LUMO energies and the energy gap (E_{gap}) are reported in Table 8. The HOMO and LUMO energies referred to vacuum were obtained using the Makov–Payne¹²¹ method. For each Si-NC, we considered $N_{\text{pdep}} = 2048$. PDEP eigenvalues are reported in Figure 12, and they clearly show that the only difference between Si-NCs of different size appears for the most screened eigenpotentials. As discussed in Section 2.3, the PDEP eigenvalues of the least screened eigenpotentials are weakly affected by the microscopic structure of the system and may likely be predicted by model screening functions. The computed G_0W_0 energy gaps for $Si_{35}H_{36}$, $Si_{87}H_{76}$, $Si_{147}H_{100}$, and $Si_{293}H_{172}$ are 6.29, 4.77, 4.21, and 3.46 eV, respectively. These results are in good agreement with those of other recent calculations using MBPT or Δ SCF method,¹²² although our

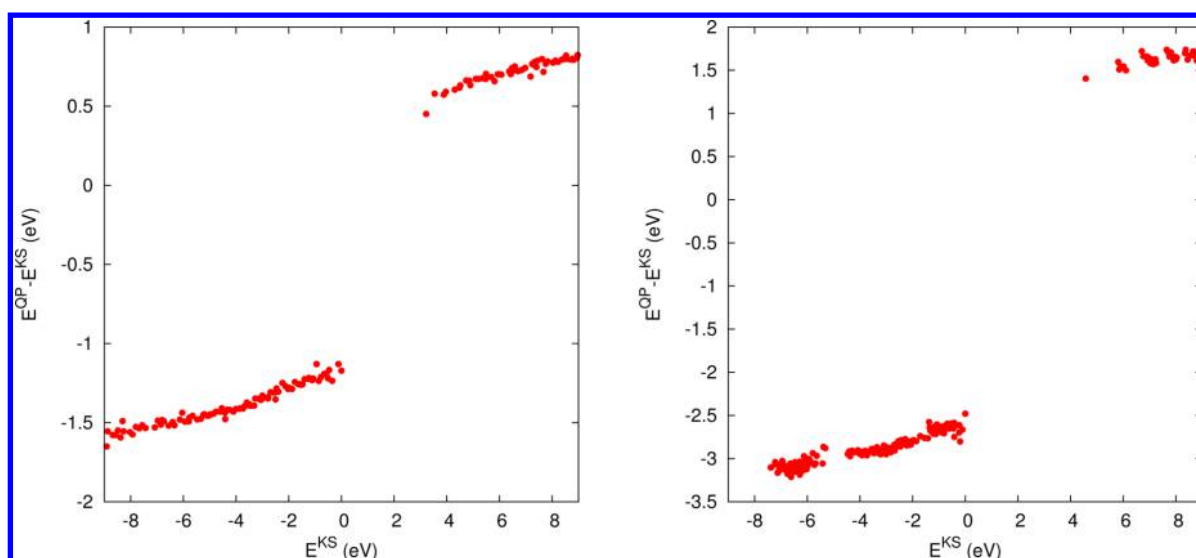


Figure 11. (Color online) Quasiparticle (QP) corrections for a configuration of amorphous Si_3N_4 (left panel) and liquid water at ambient conditions (right panel).

Table 8. Quasiparticle (QP) Energies and Energy Gap (E_{gap}) of Si Nanocrystals^a

Si-NC	N_{el}	HOMO (eV)	LUMO (eV)	E_{gap} (eV)
		G_0W_0 (PBE)	G_0W_0 (PBE)	G_0W_0 (PBE)
$\text{Si}_{35}\text{H}_{36}$	176	-7.59 (-6.08)	-1.30 (-2.57)	6.29 (3.51)
$\text{Si}_{87}\text{H}_{76}$	424	-6.69 (-5.54)	-1.92 (-2.96)	4.77 (2.58)
$\text{Si}_{147}\text{H}_{100}$	688	-6.48 (-5.44)	-2.27 (-3.15)	4.21 (2.29)
$\text{Si}_{293}\text{H}_{172}$	1344	-5.82 (-5.19)	-2.36 (-3.41)	3.46 (1.78)

^aThe Kohn–Sham eigenvalues obtained using the PBE exchange–correlation functional are reported in parentheses.

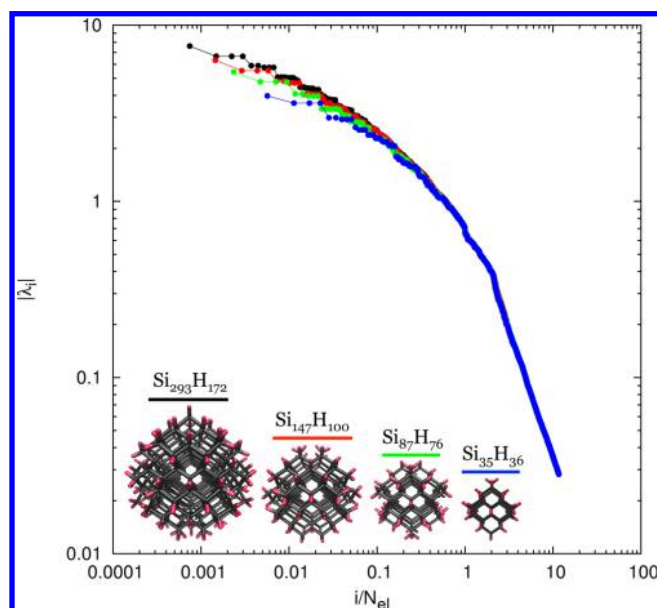


Figure 12. (Color online) PDEP eigenvalues (λ_i) for the considered Si-NCs.

computed HOMO and LUMO energies differ slightly from those reported in ref 122.

4.2. Solid/Liquid Interfaces. We now turn to discuss QP energies of extended, large systems. We considered two solid/liquid interfaces, H–Si/ H_2O and COOH–Si/ H_2O , that were recently studied by T. A. Pham et al.¹²³ to align band edges of functionalized Si(111) surfaces with water reduction and oxidation

potentials. The orthorhombic unit cell ($L_x \times L_y \times L_z$) of each system was obtained by interfacing 108 water molecules with 72 Si atoms and by terminating the solid surface exposed to water with 24 H atoms or 24 COOH groups, resulting in a $(21.97 \times 25.37 \times 63.19)$ bohr³ supercell with 1176 valence electrons and a $(21.97 \times 25.37 \times 67.53)$ bohr³ supercell with 1560 valence electrons for H–Si/ H_2O and for COOH–Si/ H_2O , respectively. Both interface geometries were extracted from a ~ 30 ps trajectory of a Car–Parrinello molecular dynamics simulation of the interface where all water molecules and atoms of the semiconductor surfaces were allowed to move (see ref 123).¹²⁴ Side views of the unit cells are shown in Figure 13, top panels. The KS electronic structure of both systems was obtained at the PBE level of theory using 85 Ry for the kinetic energy cutoff. The local density of states (LDOS) was obtained from the wave functions ψ_n and energy levels ε_n as

$$\text{LDOS}(z, E) = \sum_n \int \frac{dx}{L_x} \int \frac{dy}{L_y} |\psi_n(x, y, z)|^2 \delta(E - \varepsilon_n) \quad (67)$$

where z is the axis perpendicular to the interface and δ is the Dirac delta function. The LDOS of both systems, obtained at the PBE level of theory, is reported in Figure 13, middle panels. Those at G_0W_0 level, obtained by replacing the KS energies with QP energies in eq 67, are shown in Figure 13, bottom panels. The figures show that the method developed in Section 2 can be successfully used to compute the positions of the valence and conduction band edges of a realistic interface and hence to define an electronic thickness of the interface, by analyzing how the bulk eigenvalues are modified in proximity of

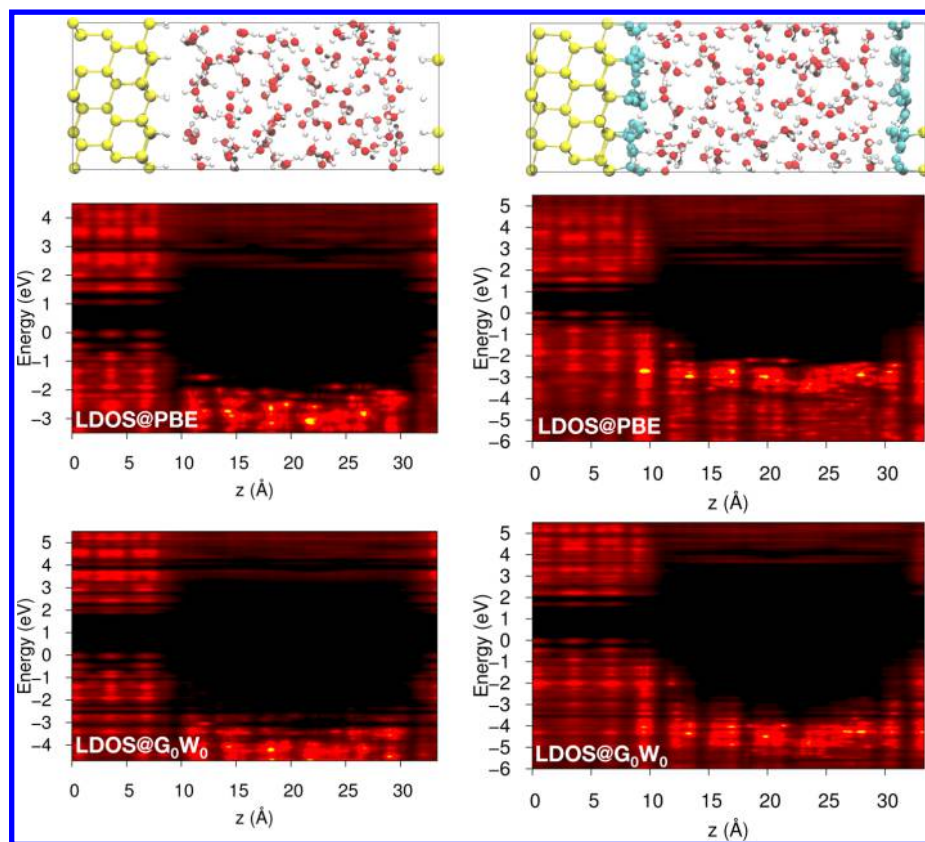


Figure 13. (Color online) The local density of states (LDOS, see text) of two solid/liquid interfaces: H-Si/H₂O (left panels) and COOH-Si/H₂O (right panels). The top panels report the side view of the unit cells. Bottom (middle) panels report the LDOS obtained using G_0W_0 (KS-DFT) energies in eq 67. A color scale that ranges from black to red is used to plot the LDOS; black areas indicate energy gap regions.

the interface. The method can of course be used for systems with impurity levels and to investigate semiconductor surfaces interfaced with aqueous solutions containing ions and to study the influence of ions on the electronic structure of the interface. The method developed here is not limited to solid/liquid interfaces and to planar geometries and has broad applicability to any complex (nanostructured) materials inclusive of heterogeneous interfaces.⁸¹

5. CONCLUSIONS

We presented a formulation of the GW method for large scale calculations carried out with the plane-wave pseudopotential method. The evaluation of polarizabilities and electronic self-energies does not require the explicit computation of virtual states. Polarizabilities and dielectric matrices were represented with a basis set composed of the eigenstates of the dielectric matrix at zero frequency, obtained using iterative procedures. In the calculation of the correlation self-energy, we avoided the use of the analytic continuation and carried out the frequency integration by means of a contour deformation technique. In addition, we presented a parallel implementation of the method that allowed us to compute the electronic properties of large nanostructures and of solid/liquid interfaces. The method is not restricted to DFT inputs obtained with semilocal functionals but can be used in conjunction with DFT calculations with hybrid functionals.

We presented a validation of the method for molecules (open and closed shell) and solids (both crystalline and amorphous) and found good agreement with data previously appeared in the literature for converged calculations. We then

applied our technique to silicon nanoparticles (up to a diameter of 2.4 nm) and solid/liquid interfaces (with up to 1560 valence electrons in the unit cell). We showed that it is now possible to carry out many body perturbation theory calculation of realistic slabs representing a semiconductor/water interface and to study in detail the modification of the bulk states at the interfaces and hence define an electronic thickness of the interface. Work is in progress to couple our GW calculations with ab initio molecular dynamics simulations of realistic materials and to include finite temperature and statistical effects in our MBPT calculations.

AUTHOR INFORMATION

Corresponding Authors

*E-mail: mgovoni@uchicago.edu.

*E-mail: gagalli@uchicago.edu.

Notes

The authors declare no competing financial interest.

ACKNOWLEDGMENTS

This work was supported by the Army Research Laboratory Collaborative Research Alliance in Multiscale Multidisciplinary Modeling of Electronic Materials (CRA-MSME, Grant No. W911NF-12-2-0023) and by DOE grant No. DE-FG02-06ER46262; the computational resources were provided by DoD Supercomputing Resource Center of the Department of Defense High Performance Computing Modernization Program. An award of computer time was provided by the Innovative and Novel Computational Impact on Theory and Experiment (INCITE) program. This research used resources

of the Argonne Leadership Computing Facility at Argonne National Laboratory, which is supported by the Office of Science of the U.S. Department of Energy under contract DE-AC02-06CH11357. Discussions with T. A. Pham and J. H. Skone are greatly acknowledged. We thank B. Rice for her help and support with computational grants of the U.S. Department of Defense's High Performance Computing Modernization Program.

REFERENCES

- (1) Onida, G.; Reining, L.; Rubio, A. *Rev. Mod. Phys.* **2002**, *74*, 601–659.
- (2) Ping, Y.; Rocca, D.; Galli, G. *Chem. Soc. Rev.* **2013**, *42*, 2437–2469.
- (3) Govoni, M.; Marri, I.; Ossicini, S. *Nat. Photonics* **2012**, *6*, 672–679.
- (4) Marri, I.; Govoni, M.; Ossicini, S. *J. Am. Chem. Soc.* **2014**, *136*, 13257–13266 PMID: 25092549.
- (5) Wippermann, S.; Vörös, M.; Gali, A.; Gygi, F.; Zimanyi, G. T.; Galli, G. *Phys. Rev. Lett.* **2014**, *112*, 106801.
- (6) Cheng, J.; Sprik, M. *Phys. Rev. B* **2010**, *82*, 081406.
- (7) Wu, Y.; Chan, M. K. Y.; Ceder, G. *Phys. Rev. B* **2011**, *83*, 235301.
- (8) Cheng, J.; Sprik, M. *Phys. Chem. Chem. Phys.* **2012**, *14*, 11245–11267.
- (9) Chen, S.; Wang, L.-W. *Chem. Mater.* **2012**, *24*, 3659–3666.
- (10) Pham, T. A.; Li, T.; Nguyen, H.-V.; Shankar, S.; Gygi, F.; Galli, G. *Appl. Phys. Lett.* **2013**, *102*, 241603.
- (11) Hohenberg, P.; Kohn, W. *Phys. Rev.* **1964**, *136*, B864–B871.
- (12) Kohn, W.; Sham, L. J. *Phys. Rev.* **1965**, *140*, A1133–A1138.
- (13) Dreizler, R. M.; Gross, E. K. U. *Density Functional Theory, An Approach to the Quantum Many-Body Problem*; Springer-Verlag: Heidelberg, 1990.
- (14) Giuliani, G.; Vignale, G. *Quantum Theory of the Electron Liquid*; Cambridge University Press: Cambridge, 2005.
- (15) Martin, R. M. *Electronic Structure, Basic Theory, and Practical Methods*; Cambridge University Press: Cambridge, 2004.
- (16) Zhang, C.; Donadio, D.; Gygi, F.; Galli, G. *J. Chem. Theory Comput.* **2011**, *7*, 1443–1449.
- (17) Gaiduk, A. P.; Zhang, C.; Gygi, F.; Galli, G. *Chem. Phys. Lett.* **2014**, *604*, 89.
- (18) Marx, D.; Hutter, J. *Ab Initio Molecular Dynamics: Basic Theory and Advanced Methods*; Cambridge University Press: Cambridge, 2005.
- (19) Alkauskas, A.; Broqvist, P.; Pasquarello, A. *Phys. Status Solidi B* **2011**, *248*, 775–789.
- (20) Chen, W.; Pasquarello, A. *Phys. Rev. B* **2013**, *88*, 115104.
- (21) Weston, L.; Janotti, A.; Cui, X. Y.; Stampfl, C.; Van de Walle, C. G. *Phys. Rev. B* **2014**, *89*, 184109.
- (22) Freysoldt, C.; Grabowski, B.; Hickel, T.; Neugebauer, J.; Kresse, G.; Janotti, A.; Van de Walle, C. G. *Rev. Mod. Phys.* **2014**, *86*, 253–305.
- (23) Skone, J. H.; Govoni, M.; Galli, G. *Phys. Rev. B* **2014**, *89*, 195112.
- (24) Lu, D.; Gygi, F. m. c.; Galli, G. *Phys. Rev. Lett.* **2008**, *100*, 147601.
- (25) Yu, P. Y.; Cardona, M. *Fundamentals of Semiconductors, Physics and Materials Properties*; Springer: New York, 2005.
- (26) Pacchioni, G. *Catal. Lett.* **2014**, *145*, 80–94.
- (27) Hybertsen, M. S.; Louie, S. G. *Phys. Rev. Lett.* **1985**, *55*, 1418–1421.
- (28) Hybertsen, M. S.; Louie, S. G. *Phys. Rev. B* **1986**, *34*, 5390–5413.
- (29) Godby, R. W.; Schlüter, M.; Sham, L. J. *Phys. Rev. B* **1988**, *37*, 10159–10175.
- (30) Farid, B.; Daling, R.; Lenstra, D.; van Haeringen, W. *Phys. Rev. B* **1988**, *38*, 7530–7534.
- (31) Engel, G. E.; Farid, B.; Nex, C. M. M.; March, N. H. *Phys. Rev. B* **1991**, *44*, 13356–13373.
- (32) Shirley, E. L.; Martin, R. M. *Phys. Rev. B* **1993**, *47*, 15404–15412.
- (33) Rohlfling, M.; Krüger, P.; Pollmann, J. *Phys. Rev. B* **1993**, *48*, 17791–17805.
- (34) Rojas, H. N.; Godby, R. W.; Needs, R. J. *Phys. Rev. Lett.* **1995**, *74*, 1827–1830.
- (35) Rohlfling, M.; Krüger, P.; Pollmann, J. *Phys. Rev. B* **1995**, *52*, 1905–1917.
- (36) Aulbur, W. G.; Jönsson, L.; Wilkins, J. W. In *Quasiparticle Calculations in Solids*; Ehrenreich, H., Spaepen, F., Eds.; Solid State Physics; Academic Press: New York, 1999; Vol. 54, pp 1–218.
- (37) Bruneval, F.; Gatti, M. In *First Principles Approaches to Spectroscopic Properties of Complex Materials*; Di Valentin, C., Botti, S., Cococcioni, M., Eds.; Topics in Current Chemistry; Springer: Berlin Heidelberg, 2014; Vol. 347, pp 99–135.
- (38) Rohlfling, M.; Louie, S. G. *Phys. Rev. B* **2000**, *62*, 4927–4944.
- (39) Nguyen, H.-V.; Pham, T. A.; Rocca, D.; Galli, G. *Phys. Rev. B* **2012**, *85*, 081101.
- (40) Pham, T. A.; Nguyen, H.-V.; Rocca, D.; Galli, G. *Phys. Rev. B* **2013**, *87*, 155148.
- (41) Pham, T. A.; Zhang, C.; Schwegler, E.; Galli, G. *Phys. Rev. B* **2014**, *89*, 060202.
- (42) Opalka, D.; Pham, T. A.; Sprik, M.; Galli, G. *J. Chem. Phys.* **2014**, *141*, 034501.
- (43) Gross, E. K. U.; Runge, E.; O, H. *Many-Particle Theory*; Hilger: London, 1991.
- (44) Hedin, L. *Phys. Rev.* **1965**, *139*, A796–A823.
- (45) Hedin, L.; Lundqvist, S. In *Effects of Electron-Electron and Electron-Phonon Interactions on the One-Electron States of Solids*; Frederick Seitz, D. T., Ehrenreich, H., Eds.; Solid State Physics; Academic Press: New York, 1970; Vol. 23; pp 1–181.
- (46) Strinati, G. *Riv. Nuovo Cimento* **1988**, *11*, 1–86.
- (47) Aryasetiawan, F.; Gunnarsson, O. *Rep. Prog. Phys.* **1998**, *61*, 237.
- (48) We use everywhere atomic Rydberg units.
- (49) The calculation of the Fock exact exchange matrix elements in reciprocal space is done employing the Gygi–Baldereschi method.¹²⁵
- (50) Although the presented methodology is general, for the purpose of this work, we have considered only normconserving pseudopotentials.¹²⁶
- (51) Wilson, H. F.; Gygi, F.; Galli, G. *Phys. Rev. B* **2008**, *78*, 113303.
- (52) Wilson, H. F.; Lu, D.; Gygi, F.; Galli, G. *Phys. Rev. B* **2009**, *79*, 245106.
- (53) The approach presented here scales as the fourth power of the system size,⁴⁰ as conventional approaches do. However the computational workload of our method represents a substantial improvement over that of conventional approaches, because of a much more favorable prefactor: the scaling is $N_{\text{occ}}^2 \times N_{\text{pdep}} \times N_{\text{pw}}$ instead of $N_{\text{occ}} \times N_{\text{empt}} \times N_{\text{pw}}^2$ where N_{occ} (N_{empt}) is the number of occupied (empty) states, N_{pw} is the number of plane waves and N_{pdep} is the number of eigenpotentials used in the PDEP expansion of the static dielectric screening.
- (54) Sternheimer, R. M. *Phys. Rev.* **1954**, *96*, 951–968.
- (55) Umari, P.; Stenuit, G.; Baroni, S. *Phys. Rev. B* **2009**, *79*, 201104.
- (56) The divergence of the Coulomb potential present in eq 23 can be numerically removed using spherical coordinates. The specific shape of the BZ is taken into account by using a Monte Carlo integration method.
- (57) In the present formulation we considered integer occupation numbers and only the dielectric response given by interband transitions.
- (58) Adler, S. L. *Phys. Rev.* **1962**, *126*, 413–420.
- (59) Wiser, N. *Phys. Rev.* **1963**, *129*, 62–69.
- (60) Baroni, S.; Resta, R. *Phys. Rev. B* **1986**, *33*, 7017–7021.
- (61) Hybertsen, M. S.; Louie, S. G. *Phys. Rev. B* **1987**, *35*, 5585–5601.
- (62) Freysoldt, C.; Eggert, P.; Rinke, P.; Schindlmayr, A.; Godby, R.; Scheffler, M. *Comput. Phys. Commun.* **2007**, *176*, 1–13.
- (63) Bruneval, F.; Gonze, X. *Phys. Rev. B* **2008**, *78*, 085125.
- (64) Berger, J. A.; Reining, L.; Sottile, F. *Phys. Rev. B* **2010**, *82*, 041103.
- (65) Kang, W.; Hybertsen, M. S. *Phys. Rev. B* **2010**, *82*, 195108.

- (66) Samsonidze, G.; Jain, M.; Deslippe, J.; Cohen, M. L.; Louie, S. G. *Phys. Rev. Lett.* **2011**, *107*, 186404.
- (67) Reining, L.; Onida, G.; Godby, R. *Phys. Rev. B* **1997**, *56*, R4301–R4304.
- (68) Lambert, H.; Giustino, F. *Phys. Rev. B* **2013**, *88*, 075117.
- (69) Soininen, J. A.; Rehr, J. J.; Shirley, E. L. *J. Phys.: Condens. Matter* **2003**, *15*, 2573.
- (70) Baroni, S.; Giannozzi, P.; Testa, A. *Phys. Rev. Lett.* **1987**, *58*, 1861–1864.
- (71) Baroni, S.; de Gironcoli, S.; Dal Corso, A.; Giannozzi, P. *Rev. Mod. Phys.* **2001**, *73*, 515–562.
- (72) Davidson, E. R. *J. Computat. Phys.* **1975**, *17*, 87–94.
- (73) Govoni, M.; Galli, G. *In preparation* 2014.
- (74) Ehrenreich, H. Electromagnetic Transport in Solids. In *The Optical Properties of Solids, Varenna Course XXXIV*; Tauc, J., Ed.; Academic Press: New York, 1966.
- (75) Hanke, W. *Adv. Phys.* **1978**, *27*, 287.
- (76) Because of the RPA, eq 18 formally corresponds to the solution of $\bar{\chi}$ when only the Hartree contribution of eq 48 is considered in eq 47.
- (77) Car, R.; Tosatti, E.; Baroni, S.; Leelaprute, S. *Phys. Rev. B* **1981**, *24*, 985–999.
- (78) Cini, M. *Topics and Methods in Condensed Matter Theory*; Springer: New York, 2007.
- (79) For the systems presented in this work, $N_{\text{Lanczos}} = 40$ yielded converged results.
- (80) Dennery, P.; Krzywicki, A. *Mathematics for Physicists*; Dover: New York, 1967.
- (81) Giantomassi, M.; Stankovski, M.; Shaltaf, R.; Grüning, M.; Bruneval, F.; Rinke, P.; Rignanese, G.-M. *Phys. Status Solidi B* **2011**, *248*, 275–289.
- (82) We note that the GW technique reported in this work replaces explicit summations over empty states present in both $G_{\text{KS}}^{\text{RPA}}$ and W_{p} with projection operations, thus avoiding the calculation of slow converging summations over empty states. However, within first order perturbation theory, in order to get the QP corrections to the energy of the KS state $\psi_{n\mathbf{k}\sigma}$ one needs to compute the mean value of the self-energy operator over that specific state and hence the wave function $\psi_{n\mathbf{k}\sigma}$ needs to be computed. Equation 65 shows that only the virtual states with energy $\epsilon_{n\mathbf{k}\sigma}$ between ϵ_{F} and $E_{n\mathbf{k}\sigma}^{\text{QP}}$ are required, which are available at no extra cost after $(\epsilon, \psi)_{n\mathbf{k}\sigma}$ have been obtained from the solution of the KS equations.
- (83) Godby, R. W.; Needs, R. J. *Phys. Rev. Lett.* **1989**, *62*, 1169–1172.
- (84) Engel, G. E.; Farid, B. *Phys. Rev. B* **1993**, *47*, 15931–15934.
- (85) Shaltaf, R.; Rignanese, G.-M.; Gonze, X.; Giustino, F.; Pasquarello, A. *Phys. Rev. Lett.* **2008**, *100*, 186401.
- (86) Stankovski, M.; Antonius, G.; Waroquiers, D.; Miglio, A.; Dixit, H.; Sankaran, K.; Giantomassi, M.; Gonze, X.; Côté, M.; Rignanese, G.-M. *Phys. Rev. B* **2011**, *84*, 241201.
- (87) Rieger, M. M.; Steinbeck, L.; White, I.; Rojas, H.; Godby, R. *Comput. Phys. Commun.* **1999**, *117*, 211–228.
- (88) Giustino, F.; Cohen, M. L.; Louie, S. G. *Phys. Rev. B* **2010**, *81*, 115105.
- (89) Giannozzi, P.; Baroni, S.; Bonini, N.; Calandra, M.; Car, R.; Cavazzoni, C.; Ceresoli, D.; Chiarotti, G. L.; Cococcioni, M.; Dabo, I.; Corso, A. D.; de Gironcoli, S.; Fabris, S.; Fratesi, G.; Gebauer, R.; Gerstmann, U.; Gougoussis, C.; Kokalj, A.; Lazzeri, M.; Martin-Samos, L.; Marzari, N.; Mauri, F.; Mazzarello, R.; Paolini, S.; Pasquarello, A.; Paulatto, L.; Sbraccia, C.; Scandolo, S.; Sclauzero, G.; Seitonen, A. P.; Smogunov, A.; Umari, P.; Wentzcovitch, R. M. *J. Phys.: Condens. Matter* **2009**, *21*, 395502.
- (90) Curtiss, L. A.; Redfern, P. C.; Raghavachari, K.; Pople, J. A. *J. Chem. Phys.* **1998**, *109*, 42–55.
- (91) Rostgaard, C.; Jacobsen, K. W.; Thygesen, K. S. *Phys. Rev. B* **2010**, *81*, 085103.
- (92) Caruso, F.; Rinke, P.; Ren, X.; Scheffler, M.; Rubio, A. *Phys. Rev. B* **2012**, *86*, 081102.
- (93) Blase, X.; Attaccalite, C.; Olevano, V. *Phys. Rev. B* **2011**, *83*, 115103.
- (94) Ren, X.; Rinke, P.; Blum, V.; Wieferink, J.; Tkatchenko, A.; Sanfilippo, A.; Reuter, K.; Scheffler, M. *New J. Phys.* **2012**, *14*, 053020.
- (95) Bruneval, F.; Marques, M. A. L. *J. Chem. Theory Comput.* **2013**, *9*, 324–329.
- (96) Sharifzadeh, S.; Tamblyn, I.; Doak, P.; Darancet, P.; Neaton, J. *Eur. Phys. J. B* **2012**, *85*, 323.
- (97) NIST Computational Chemistry Comparison and Benchmark Database, NIST Standard Reference Database Number 101, Release 16a; Johnson, R. D., III, Ed.; NIST: Gaithersburg, MD, Aug. 2013; <http://cccbdb.nist.gov/>.
- (98) In order to prevent the occurrence of spurious size effects in the computation of VIPs, we referred the KS eigenvalues to the vacuum level. The vacuum level was computed as the spherical average of the electrostatic potential over a sphere of diameter equal to the edge of the cubic simulation cell and centered on the ionic pseudocharge position. Because in our G_0W_0 calculations we did not update the wave functions and thus the charge density, the vacuum level was not recomputed when QP corrections were added to KS eigenvalues.
- (99) For open shell molecules, the VIPs obtained with the LDA (PBE) exchange correlation functional have been obtained using LDA (PBE) norm-conserving pseudopotentials. Simulations were performed considering collinear spins, a cell of edge 30 bohr and a kinetic energy cutoff of 85 Ry.
- (100) Caruso, F.; Rinke, P.; Ren, X.; Rubio, A.; Scheffler, M. *Phys. Rev. B* **2013**, *88*, 075105.
- (101) Krukau, A. V.; Vydrov, O. A.; Izmaylov, A. F.; Scuseria, G. E. *J. Chem. Phys.* **2006**, *125*, 224106.
- (102) Perdew, J. P.; Burke, K.; Ernzerhof, M. *Phys. Rev. Lett.* **1996**, *77*, 3865–3868.
- (103) Ernzerhof, M.; Scuseria, G. E. *J. Chem. Phys.* **1999**, *110*, 5029–5036.
- (104) Aulbur, W. G.; Städele, M.; Görling, A. *Phys. Rev. B* **2000**, *62*, 7121–7132.
- (105) Stephens, P. J.; Devlin, F. J.; Chabalowski, C. F.; Frisch, M. J. *J. Phys. Chem.* **1994**, *98*, 11623–11627.
- (106) Klasinc, L.; Sabljic, A.; Kluge, G.; Rieger, J.; Scholz, M. *J. Chem. Soc., Perkin Trans. 2* **1982**, 539–543.
- (107) Garbuio, V.; Cascella, M.; Reining, L.; Sole, R. D.; Pulci, O. *Phys. Rev. Lett.* **2006**, *97*, 137402.
- (108) Bauer, J. *Phys. Status Solidi A* **1977**, *39*, 411–418.
- (109) Fleszar, A.; Hanke, W. *Phys. Rev. B* **1997**, *56*, 10228–10232.
- (110) Rohlfing, M.; Krüger, P.; Pollmann, J. *Phys. Rev. B* **1993**, *48*, 17791–17805.
- (111) Lebègue, S.; Arnaud, B.; Alouani, M.; Blochl, P. E. *Phys. Rev. B* **2003**, *67*, 155208.
- (112) Hellwege, K. H.; Green, L. C. *Landolt-Börnstein, Numerical Data and Functional Relationships in Science and Technology, New Series*; Springer: Berlin, 1982; Vol. III, 17a and 22a.
- (113) Ortega, J. E.; Himpel, F. J. *Phys. Rev. B* **1993**, *47*, 2130–2137.
- (114) Hulthén, R.; Nilsson, N. *Solid State Commun.* **1976**, *18*, 1341–1343.
- (115) Straub, D.; Ley, L.; Himpel, F. J. *Phys. Rev. Lett.* **1985**, *54*, 142–145.
- (116) Spicer, W. E.; Eden, R. C. In *Proc. Ninth Int. Conf. Phys. Semiconductors*, Moscow; Ryvkin, S. M., Ed.; 1968; Vol. 1.
- (117) Wachs, A. L.; Miller, T.; Hsieh, T. C.; Shapiro, A. P.; Chiang, T.-C. *Phys. Rev. B* **1985**, *32*, 2326–2333.
- (118) Lambrecht, W. R. L.; Segall, B.; Yoganathan, M.; Suttrop, W.; Devaty, R. P.; Choyke, W. J.; Edmond, J. A.; Powell, J. A.; Alouani, M. *Phys. Rev. B* **1994**, *50*, 10722–10726.
- (119) Lee, H. J.; Jurel, L. Y.; Woolley, J. C.; Thorpe, A. J. S. *Phys. Rev. B* **1980**, *21*, 659–669.
- (120) We have indicated in parentheses the diameter of each Si nanocrystal.
- (121) Makov, G.; Payne, M. C. *Phys. Rev. B* **1995**, *51*, 4014–4022.
- (122) Neuhauser, D.; Gao, Y.; Arntsen, C.; Karshenas, C.; Rabani, E.; Baer, R. *Phys. Rev. Lett.* **2014**, *113*, 076402.
- (123) Pham, T. A.; Lee, D.; Schwegler, E.; Galli, G. *J. Am. Chem. Soc.* **2014**, *136*, 17071–17077 PMID: 25402590.

(124) The comparison between the results reported here and those of Figure 11 of ref 41 is not straightforward for several reasons: (i) here we just reported results for one snapshot, arbitrarily extracted from a ~ 30 ps simulation, as a proof of principle that G_0W_0 calculations can indeed be done. (ii) The difference between results obtained by doing G_0W_0 calculations of slabs, as opposed to using values of the band edges of water and functionalized Si computed in the bulk, as done in ref 123, remains to be explored and will be the subject of further investigation in a subsequent work.

(125) Gygi, F.; Baldereschi, A. *Phys. Rev. B* **1986**, *34*, 4405–4408.

(126) Focher, P.; Lastri, A.; Covi, M.; Bachelet, G. B. *Phys. Rev. B* **1991**, *44*, 8486–8495.